

## Uncertainty quantification confirms unreliable extrapolation toward high pressures for united-atom Mie $\lambda$ -6 force field

Richard A. Messerly,<sup>1, a)</sup> Michael R. Shirts,<sup>2, b)</sup> and Andrei F. Kazakov<sup>1, c)</sup>

<sup>1)</sup>*Thermodynamics Research Center, National Institute of Standards and Technology, Boulder, Colorado, 80305*

<sup>2)</sup>*Department of Chemical and Biological Engineering, University of Colorado, Boulder, Colorado, 80309*

Molecular simulation results at extreme temperatures and pressures can supplement experimental data when developing fundamental equations of state. Since most force fields are optimized to agree with vapor-liquid equilibria (VLE) properties, however, the reliability of the molecular simulation results depends on the validity/transferability of the force field at higher temperatures and pressures. As demonstrated in this study, although state-of-the-art united-atom Mie  $\lambda$ -6 potentials for normal and branched alkanes provide accurate estimates for VLE, they tend to over-predict pressures for dense supercritical fluids and compressed liquids. The physical explanation for this observation is that the repulsive barrier is too steep for the “optimal” united-atom Mie  $\lambda$ -6 potential parameterized with VLE properties. Bayesian inference confirms that no feasible combination of non-bonded parameters ( $\epsilon$ ,  $\sigma$ , and  $\lambda$ ) is capable of simultaneously predicting saturated vapor pressures, saturated liquid densities, and pressures at high temperatures and densities. This conclusion has both practical and theoretical ramifications, as more realistic non-bonded potentials may be required for accurate extrapolation to high pressures of industrial interest.

Keywords: Transferability, Molecular Simulation, Bayesian Inference, Markov Chain Monte Carlo

---

<sup>a)</sup>Electronic mail: [richard.messerly@nist.gov](mailto:richard.messerly@nist.gov)

<sup>b)</sup>Electronic mail: [michael.shirts@colorado.edu](mailto:michael.shirts@colorado.edu)

<sup>c)</sup>Electronic mail: [andrei.kazakov@nist.gov](mailto:andrei.kazakov@nist.gov)

## I. INTRODUCTION

An accurate understanding of the relationship between pressure ( $P$ ), density ( $\rho$ ), and temperature ( $T$ ) and caloric properties (such as internal energy  $U$ ) for a given compound is essential for designing industrial chemical processes. Fundamental equations of state (FEOS), such as those based on the Helmholtz free energy, are a powerful approach for estimating  $P\rho T$  behavior and caloric properties. For example, the National Institute of Standards and Technology (NIST) Reference Fluid Properties (REFPROP) currently provides FEOS for approximately one hundred fifty chemical species.<sup>1</sup> Unfortunately, most compounds do not have sufficient *reliable* experimental data covering a wide range of pressures, densities, and temperatures to develop a highly-accurate FEOS. Since FEOS are semi-empirical and have 50 to 100 fitting parameters, the FEOS predictions can result in large errors at temperatures and pressures that are significantly higher than those used in parameterizing the FEOS, which are typically near or below the critical temperature and pressure. Therefore, improvement in an FEOS at high temperatures and pressures necessitates additional data for those conditions.

The lack of experimental data at high temperatures and pressures, especially, is attributed to the inherent safety, cost, and complexity of such experiments. By contrast, molecular simulation (i.e. Monte Carlo, MC, and molecular dynamics, MD) methods at high temperatures and pressures do not suffer from any of these limitations. Therefore, in principle, molecular simulation can aid in developing FEOS.<sup>2-6</sup> Although it is possible to fit an FEOS to just molecular simulation results, most studies implement hybrid data sets, i.e. from both experiment and molecular simulation.<sup>7</sup>

For example, several recent studies supplement experimental data with molecular simulation results at temperatures and pressures beyond the range of available experimental temperatures and pressures.<sup>8-11</sup> Specifically, experimental data were available for temperatures and pressures up to 580 K and 130 MPa, 590 K and 180 MPa, 450 K and 2 MPa, and 560 K and 100 MPa for hexamethyldisiloxane,<sup>8</sup> octamethylcyclotetrasiloxane,<sup>9</sup> ethylene

---

Contribution of NIST, an agency of the United States government; not subject to copyright in the United States.

oxide,<sup>11</sup> and 1,2-dichloroethane,<sup>10</sup> respectively. Molecular simulations were performed for these compounds at temperatures and pressures up to 1200 K and 600 MPa, 1200 K and 520 MPa, 1000 K and 700 MPa, 1000 K and 1200 MPa, respectively. The inclusion of these simulation results improved the performance of the FEOS at extreme temperatures and pressures.

While previous studies have focused on small/hazardous compounds, the present study investigates normal and branched alkanes. Hydrocarbons are a fundamental feed-stock for many petrochemical processes and, therefore, a large body of experimental data exist covering a wide range of  $P\rho T$  phase space for some alkanes. For these reasons, REFPROP provides highly-accurate FEOS for several hydrocarbons, most of which are shorter-chains (less than 20 carbons) with limited branching (i.e. only methyl branches). The use of hybrid data sets is an appealing approach to develop FEOS for industrially relevant hydrocarbons with minimal experimental data, i.e. those with longer chain-lengths or a higher degree of branching.

The primary limitation for implementing molecular simulation at extreme temperatures and pressures is whether or not the force field, which is typically parameterized using VLE data, is reliable at those conditions. For example, it was demonstrated that VLE-optimized force fields for small compounds, such as noble gases, hydrogen sulfide, and hydrogen chloride, do adequately represent the homogeneous fluid region.<sup>7</sup> In this study, we investigate how well the traditional force fields for predicting VLE of normal and branched alkanes extrapolate to higher temperatures and pressures, i.e dense supercritical fluids and compressed liquids. This analysis is performed for four normal and four branched alkanes by comparing the simulated compressibility factor ( $Z$ ) with the REFPROP correlations. Note that the simulation conditions do not go beyond the range of REFPROP validity for the respective compounds, so that we can assume the REFPROP correlations are reliable.

The most accurate force fields for estimating hydrocarbon VLE properties, such as  $\rho_1^{\text{sat}}$  and  $P_v^{\text{sat}}$ , are the Transferable Potentials for Phase Equilibria (TraPPE)<sup>12,13</sup> (and, especially, the recent TraPPE-2<sup>14</sup>), Errington,<sup>15</sup> fourth generation anisotropic-united-atom (AUA4),<sup>16,17</sup> Potoff,<sup>18,19</sup> and Transferable anisotropic Mie potential (TAMie).<sup>20,21</sup> Note that

each is either an united-atom (UA) or an anisotropic-united-atom (AUA) force field. In contrast with the more computationally expensive all-atom (AA) approach, both UA and AUA models group the hydrogen interaction sites with their neighboring carbon atom. Although an AA force field should, in principle, be able to yield more accurate VLE results, it is much easier to locate the “true” optimal parameter set for UA and AUA force fields since fewer (highly correlated) parameters are optimized simultaneously.

In addition to the division between UA and AUA force fields, the existing force fields differ in the non-bonded functional form and corresponding parameters. The TraPPE, TraPPE-2, and AUA4 force fields use a Lennard-Jones (LJ) 12-6 potential, while the Potoff and TAMie force fields use the Mie  $\lambda$ -6 (or generalized Lennard-Jones) potential, and the Errington force field uses the Buckingham exponential-6 (Exp-6) potential. The Mie  $\lambda$ -6 potential is:<sup>22</sup>

$$u^{\text{vdw}}(\epsilon, \sigma, \lambda; r) = \left( \frac{\lambda}{\lambda - 6} \right) \left( \frac{\lambda}{6} \right)^{\frac{6}{\lambda - 6}} \epsilon \left[ \left( \frac{\sigma}{r} \right)^\lambda - \left( \frac{\sigma}{r} \right)^6 \right] \quad (1)$$

where  $u^{\text{vdw}}$  is the van der Waals interaction,  $\sigma$  is the distance ( $r$ ) where  $u^{\text{vdw}} = 0$ ,  $-\epsilon$  is the energy of the potential at the minimum (i.e.  $u^{\text{vdw}} = -\epsilon$  and  $\frac{du^{\text{vdw}}}{dr} = 0$  for  $r = r_{\min}$ ), and  $\lambda$  is the repulsive exponent.

The Buckingham exponential-6 model is:<sup>15</sup>

$$u^{\text{vdw}}(\epsilon, r_{\min}, \alpha; r) = \begin{cases} \frac{\epsilon}{1 - \frac{6}{\alpha}} \left[ \frac{6}{\alpha} \exp \left( \alpha \left[ 1 - \frac{r}{r_{\min}} \right] \right) - \left( \frac{r_{\min}}{r} \right)^6 \right] & \text{for } r > r_{\max} \\ \infty & \text{for } r < r_{\max} \end{cases} \quad (2)$$

where  $u^{\text{vdw}}$ ,  $\epsilon$ , and  $r$  are the same as in Equation 1,  $r_{\min}$  is the distance that corresponds to the minimum in the potential (i.e.  $u^{\text{vdw}}(r_{\min}) = -\epsilon$ ),  $\alpha$  is a Buckingham exponential-6 parameter, and  $r_{\max}$  is the smallest positive value for which  $\frac{du^{\text{vdw}}}{dr} = 0$ .

The three-parameter Mie  $\lambda$ -6 and Exp-6 potentials are more flexible than the two-parameter LJ 12-6 potential as an additional adjustable parameter controls the steepness of the repulsive barrier. Note that the Mie  $\lambda$ -6 potential reduces to the LJ 12-6 potential for  $\lambda = 12$ . Therefore, the LJ 12-6 potential can be considered a special subclass of the Mie  $\lambda$ -6 potential.

Previous work demonstrated that the UA LJ 12-6 potential cannot adequately estimate

both  $\rho_1^{\text{sat}}$  and  $P_v^{\text{sat}}$  for  $n$ -alkanes.<sup>23,24</sup> For this reason, the TraPPE-UA force field was primarily developed to agree with  $\rho_1^{\text{sat}}$  (and the critical temperature,  $T_c$ ).<sup>12</sup> By contrast, accurate prediction of both  $\rho_1^{\text{sat}}$  and  $P_v^{\text{sat}}$  over a wide temperature range is possible by varying the repulsive exponent of the LJ potential (i.e. the Mie  $\lambda$ -6 potential). Although an attractive exponent of 6 has a strong theoretical basis,  $\lambda = 12$  (LJ 12-6) is a historical artifact that was chosen primarily for computational purposes (see pages 18, 140 to 143 of Reference 25).

Typically, when parameterized to VLE data, the optimal value of  $\lambda$  is greater than 12 with a corresponding increase in the well depth ( $\epsilon$ ). Specifically, for most hydrocarbons, the Potoff UA force field<sup>18,19</sup> uses  $\lambda = 16$  while the TAMie force field<sup>20</sup> uses  $\lambda = 14$ . Gordon also demonstrated that reliable viscosities can be obtained from a UA Mie  $\lambda$ -6 model for  $n$ -alkanes by using  $\lambda = 14$  and  $\lambda = 20$  for the  $\text{CH}_3$  and  $\text{CH}_2$  sites, respectively (note the subtle difference in how Gordon defines the Mie  $\lambda$ -6 potential, a.k.a. “mod- $n$ -6”).<sup>26</sup> However, it is important to note that Gordon and Galliéro et al. report  $\lambda$  values of 11 and 10, respectively, for UA methane when optimized with viscosity data.<sup>26,27</sup>

There are some theoretical concerns that increasing the repulsive exponent might have some undesirable consequences, especially at high pressures, where particles will spend more time with very short pairwise distances than at VLE conditions. For example, References 28–30 demonstrate that neither an all-atom LJ 12-6 or an all-atom LJ 9-6 is adequate to reproduce high-level *ab initio* calculations of  $n$ -alkanes ranging from methane to  $n$ -butane. The studies of Rowley et al. suggest a modified-Morse potential is necessary for accurate representation of *ab initio* dimer energies.<sup>28,29</sup> Hayes et al. confirms these results while also emphasizing that the short-range repulsive forces, which are most important when computing high pressures in molecular simulation, are poorly represented with an AA LJ 12-6 or an AA LJ 9-6 model.<sup>30</sup> Specifically, the LJ 12-6 potential is too steep, and only slight improvement in the repulsive region is observed for the LJ 9-6 potential. Note that Hayes et al. also highlights deficiencies in the repulsive region for the Buckingham exponential-6 potential.

Recently, Kulakova et al. used Bayesian inference to conclude that experimental data for argon, specifically the liquid and vapor radial distribution functions at varying temperatures and densities, support  $\lambda$  values between 6 and 10, while argon dimer *ab initio*

energies support  $\lambda$  values between 12 and 14.<sup>31</sup> They suggest that these larger values of  $\lambda$  should not be used for liquid phase simulations. By contrast, two other studies of noble gases, including argon, support  $\lambda \geq 12$ .<sup>27,32</sup> Specifically, Mick et al. reports a 13-6 potential for argon, while Galliéro et al. states that the 12-6 potential is superior for argon than the 10-6, 14-6, 16-6, 18-6, and 20-6 potentials. The likely explanation for this discrepancy is the choice of experimental data. The optimal value of  $\lambda$  from Kulakova et al. is based on the radial distribution function, while Galliéro et al. used viscosity and pressure, and Mick et al. utilized VLE data.

Structural properties, such as the radial distribution function, and *ab initio* calculations provide considerable insight into the true repulsive barrier.<sup>27,31</sup> However, the “correct” value of  $\lambda$  does not guarantee adequate prediction of VLE and/or  $P\rho T$  behavior. This is primarily because the Mie  $\lambda$ -6 potential is only an approximation to the real potential and, thus, it is not flexible enough to agree with both the repulsive and attractive regions. Instead, only the region that is most sensitive to the target experimental data will be adequately represented. For example, high pressure properties are sensitive to extremely close-range interactions ( $r < 0.8\sigma$ ), while such distances are rarely sampled with VLE simulations and, thereby, do not impact VLE properties. Furthermore, the “optimal”  $\lambda$  is an “effective optimal” as it accounts for numerous model assumptions, such as pair-wise additivity (i.e. excluding three-, four-, etc. body interactions) or the lack of explicit hydrogens. For these reasons, despite theoretical evidence that the repulsive barrier should be softer than  $\lambda = 12$ , a UA Mie  $\lambda$ -6 potential is simply not capable of predicting VLE properties of ethane for  $\lambda < 12$  (see Figures 1 and 2 of Reference 18).

The purpose of this study is to determine whether or not the UA Mie  $\lambda$ -6 model is adequate for predicting *both* VLE and  $P\rho T$  at high temperatures and pressures for alkanes. Although the theoretical results discussed previously for noble gases and all-atom *n*-alkane models are not necessarily applicable to UA models for normal and branched alkanes, the working hypothesis based on the literature is that a UA Mie  $\lambda$ -6 potential parameterized with VLE data is too repulsive and, thus, performs poorly at high pressures. This assessment is of practical engineering importance for deciding whether or not UA Mie  $\lambda$ -6 force fields should be used when developing fundamental equations of state for

alkanes based on hybrid data sets.

The outline for this study is the following. Section II discusses the simulation and force field details. Section III is a case study for normal and branched alkanes using the existing force fields developed based on VLE properties. Section IV explains how Bayesian inference is employed to investigate the adequacy of the UA Mie  $\lambda$ -6 potential. Section V presents the results from the Bayesian analysis with recommendations and limitations in Section VI. Section VII reports the primary conclusions of this study.

## II. MOLECULAR DYNAMICS

### A. Simulation Details

Four normal and four branched alkanes of varying chain-length and degree of branching are simulated in this study. Specifically, we simulate ethane, propane, *n*-butane, *n*-octane, isobutane (2-methylpropane), isohexane (2-methylpentane), isooctane (2,2,4-trimethylpentane), and neopentane (2,2-dimethylpropane). These compounds were chosen to represent a diverse set of the normal and branched alkanes available in REFPROP.<sup>1,33–38</sup>

Molecular dynamics simulations for this study are performed in the *NVT* ensemble (constant number of molecules, *N*, constant volume, *V*, and constant temperature, *T*) using GROMACS version 2018.<sup>39</sup> Each simulation uses the velocity Verlet integrator with a 2 fs time-step, 1.4 nm cut-off for non-bonded interactions with tail corrections for energy and pressure, Nosé-Hoover thermostat with a thermostat time constant of 1 ps,<sup>40</sup> and fixed bond-lengths constrained using LINear Constraint Solver (LINCS) with a LINCS-order of eight.<sup>41,42</sup> Note that GROMACS non-bonded tail corrections assume that the long-range contribution from the  $r^{-\lambda}$  term is negligible compared to the  $r^{-6}$  term. A comparison between the energies and pressures obtained with GROMACS and other (slower) simulation packages verified that the small error introduced with this approximation does not significantly affect our results. For this reason, we did not attempt to modify the GROMACS default tail correction values to include the  $r^{-\lambda}$  contribution. Also, Coulombic interactions are not computed as none of the force fields require partial charges for the

compounds studied.

The equilibration time is 0.1 ns for ethane and propane, 0.2 ns for *n*-butane, and 0.5 ns for all other compounds. The production time is 1 ns for ethane, 2 ns for propane and *n*-butane, and 4 ns for all other compounds. Replicate simulations are performed for *n*-octane to validate that a single MD run of this length agrees with the average of several replicates, to within the combined uncertainty. A system size of 400 molecules is used for ethane, propane, and *n*-butane, while all other compounds use 800 molecules. Example input files are provided as Supporting Information.

The specific state points for each compound studied are depicted in Figure 1 (for tabulated values, see Section SII of Supporting Information). These state points correspond to the recommended conditions for the isothermal isochoric integration (ITIC) algorithm discussed in Section IV.<sup>43–45</sup> Simulations are performed along a supercritical isotherm (with a reduced temperature,  $T_r \approx 1.2$ ) and five saturated liquid density isochores ( $\rho^{\text{IC}}$ ). Nine densities are simulated along the supercritical isotherm ( $T^{\text{IT}}$ ). Three temperatures are simulated along each isochore, namely,  $T^{\text{IT}}$ , the REFPROP saturation temperature ( $T^{\text{sat}}$ ), and  $2/(1/T^{\text{IT}} + 1/T^{\text{sat}})$ . Since five of the isotherm densities correspond to the five different  $\rho^{\text{IC}}$  values, a total of 19 simulations are performed for each compound and force field.

## B. Force field

A united-atom (UA) or anisotropic-united-atom (AUA) representation is used for each compound studied. UA models assume that the UA interaction site is that of the carbon atom, while AUA models assume that the AUA interaction site is displaced from the carbon atom towards the hydrogen atom(s). Note that TraPPE and Potoff are UA force fields while the TraPPE-2, Errington, AUA4, and TAMie are AUA force fields.

The UA and AUA groups required for normal and branched alkanes are  $\text{sp}^3$  hybridized  $\text{CH}_3$ ,  $\text{CH}_2$ ,  $\text{CH}$ , and  $\text{C}$  sites. For most literature models, a single (transferable) parameter set is assigned for each interaction site. However, two exceptions exist for the force fields studied. First, TAMie implements a different set of  $\text{CH}_3$  parameters for



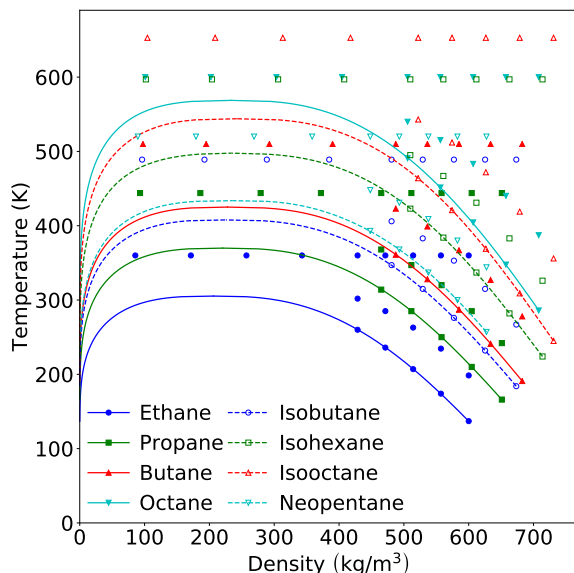


FIG. 1. State points simulated for ethane, propane, *n*-butane, *n*-octane, isobutane, isohexane, isooctane, and neopentane. A total of 19 simulations are performed: nine densities along the supercritical isotherm and two temperatures along five liquid density isochores. Filled symbols and solid lines correspond to *n*-alkanes, while empty symbols and dashed lines correspond to branched alkanes. The REFPROP saturation curve for each compound is included as a reference.<sup>1,33–38</sup>

ethane. Second, Potoff reports a “generalized” and “short/long” (S/L) CH and C parameter set. The Potoff “generalized” CH and C parameter set is an attempt at a completely transferable set. However, since the “generalized” parameters performed poorly for some compounds, the S/L parameter set was proposed, where the “short” and “long” parameters are implemented when the number of carbons in the backbone is  $\leq 4$  and  $> 4$ , respectively.

A fixed bond-length is used for each bond between UA or AUA sites. Although TAMie is an AUA force field, only the terminal  $\text{CH}_3$  sites have a displacement in the interaction site. For example, Figure 2 depicts both the UA and AUA representations of isooctane when only terminal  $\text{CH}_3$  interaction sites are displaced from the carbon center. This convention is much simpler to implement than other AUA approaches (such as AUA4) where non-terminal (i.e.  $\text{CH}_2$  and CH) interaction sites also have a displacement distance. For

this reason, we do not attempt to simulate the AUA4 force field for any compounds containing  $\text{CH}_2$  and  $\text{CH}$  interaction sites. For the compounds and force fields simulated, the anisotropic displacement in a terminal interaction site (i.e.  $\text{CH}_3$ ) is treated simply as a longer effective bond-length (see Table I). The bond-length for all non-terminal sites is 0.154 nm, except for the Errington Exp-6 force field which uses 0.1535 nm for  $\text{CH}_2\text{-CH}_2$  bonds.

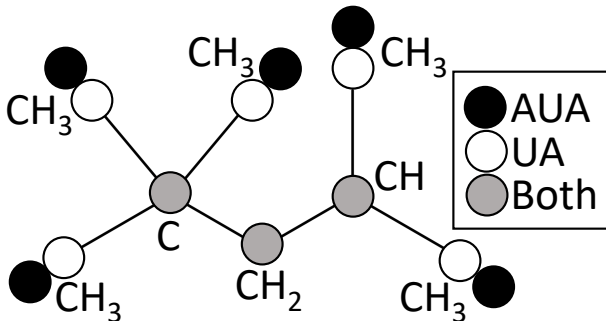


FIG. 2. Comparison between AUA and UA representations of isooctane. AUA force fields have the same complexity as UA force fields if only the terminal ( $\text{CH}_3$ ) sites have an anisotropic displacement, i.e. a longer effective bond-length. Note that the AUA4 approach requires a more complicated displacement of  $\text{CH}_2$  and  $\text{CH}$  sites than that depicted here.<sup>16</sup>

The angle and dihedral energies are computed using the same functional forms for each force field. Angular bending interactions are evaluated using a harmonic potential:

$$u^{\text{bend}} = \frac{k_\theta}{2} (\theta - \theta_0)^2 \quad (3)$$

where  $u^{\text{bend}}$  is the bending energy,  $\theta$  is the instantaneous bond angle,  $\theta_0$  is the equilibrium bond angle (see Table II), and  $k_\theta$  is the harmonic force constant with  $k_\theta/k_B = 62500 \text{ K/rad}^2$  for all bonding angles, where  $k_B$  is the Boltzmann constant.

Dihedral torsional interactions are determined using a cosine series:

$$u^{\text{tors}} = c_0 + c_1[1 + \cos \phi] + c_2[1 - \cos 2\phi] + c_3[1 + \cos 3\phi] \quad (4)$$

where  $u^{\text{tors}}$  is the torsional energy,  $\phi$  is the dihedral angle and  $c_i$  are the Fourier constants (see Table III). Note that the Errington  $c_i$  values for  $\text{CH}_x\text{-CH}_2\text{-CH}_2\text{-CH}_y$  are a factor of two less than those reported in Table III.<sup>15</sup>

TABLE I. Effective bond-lengths in units of nm for terminal (CH<sub>3</sub>) UA or AUA interaction sites. Empty table entries for Exp-6<sup>15</sup> and TraPPE-2<sup>14</sup> denote that the force field does not contain the corresponding interaction site type. Empty table entries in AUA4<sup>16</sup> arise because this force field uses a more complicated construction than the simple effective bond-length approach. Specifically, AUA4 requires CH<sub>2</sub> and CH interaction sites that are not along the C-C bond axis.

Bond	TraPPE, Potoff	TAMie	Exp-6	AUA4	TraPPE-2
CH <sub>3</sub> -CH <sub>3</sub>	0.154	0.194	0.1839	0.1967	0.230
CH <sub>3</sub> -CH <sub>2</sub>	0.154	0.174	0.1687	–	–
CH <sub>3</sub> -CH	0.154	0.174	–	–	–
CH <sub>3</sub> -C	0.154	0.174	–	0.1751	–

TABLE II. Equilibrium bond angles ( $\theta_0$ ).<sup>13</sup>  $x$  and  $y$  are values between 0-3.

Bending sites	$\theta_0$ (degrees)
CH <sub><math>x</math></sub> -CH <sub>2</sub> -CH <sub><math>y</math></sub>	114.0
CH <sub><math>x</math></sub> -CH-CH <sub><math>y</math></sub>	112.0
CH <sub><math>x</math></sub> -C-CH <sub><math>y</math></sub>	109.5

TABLE III. Fourier constants ( $c_i/k_B$ ) in units of K.<sup>13</sup>  $x$  and  $y$  are values between 0-3.

Torsion sites	$c_0/k_B$	$c_1/k_B$	$c_2/k_B$	$c_3/k_B$
CH <sub><math>x</math></sub> -CH <sub>2</sub> -CH <sub>2</sub> -CH <sub><math>y</math></sub>	0.0	355.03	-68.19	791.32
CH <sub><math>x</math></sub> -CH <sub>2</sub> -CH-CH <sub><math>y</math></sub>	-251.06	428.73	-111.85	441.27
CH <sub><math>x</math></sub> -CH <sub>2</sub> -C-CH <sub><math>y</math></sub>	0.0	0.0	0.0	461.29

Non-bonded interaction energies and forces between sites located in two different molecules or separated by more than three bonds are calculated using either a Lennard-

Jones 12-6, Mie  $\lambda$ -6, or Buckingham Exponential-6 potential (see Equations 1-2). Figure 3 compares the energy and force of the LJ 12-6, Mie 9-6, Mie 16-6, and Exp-6 (for  $\alpha = 16$  and 22) using the same values of  $\epsilon$  and  $r_{\min}$ .

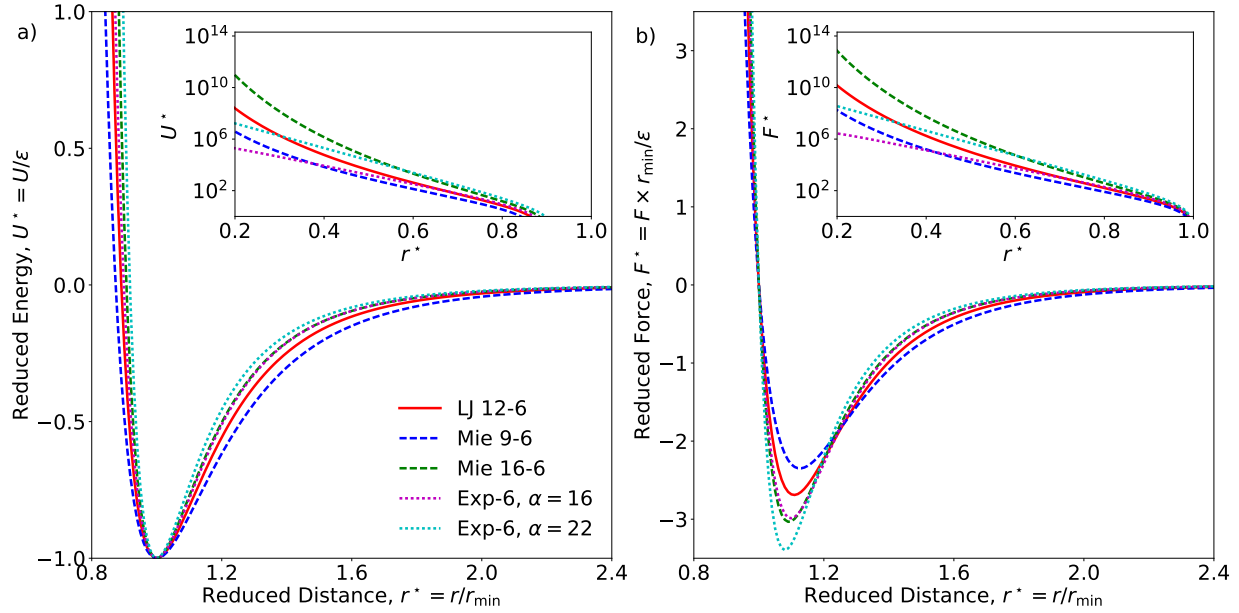


FIG. 3. Comparison between Equations 1 and 2. Short distance forces increase and energy wells become more narrow with increasing  $\lambda$  and  $\alpha$ . Panels a) and b) plot the reduced energy ( $U^*$ ) and force ( $F^*$ ) with respect to the reduced distance ( $r^*$ ), where the energy and distance are scaled by  $\epsilon$  and  $r_{\min}$ , respectively.

The non-bonded LJ 12-6 or Mie  $\lambda$ -6 force field parameters for TraPPE, TraPPE-2, Potoff, AUA4, and TAMie are provided in Table IV. Note that, for computational purposes, a common practice to date is to use integer values of  $\lambda$  in Equation 1.

The Errington Exp-6 non-bonded parameters are found in Table V. Note that Errington reported values for  $\epsilon$ ,  $\sigma$ , and  $\alpha$ . We computed  $r_{\min}$  and  $r_{\max}$  to facilitate compatibility with Equation 2 and future validation of our results.

Non-bonded interactions between two different site types (i.e. cross-interactions) are determined using Lorentz-Berthelot combining rules<sup>25</sup> for  $\epsilon$  and  $\sigma$ , an arithmetic mean for the repulsive exponent  $\lambda$  (as recommended in Reference 18), and a geometric mean for  $\alpha$

TABLE IV. Non-bonded (intermolecular) parameters for TraPPE<sup>12,13</sup> (and TraPPE-2<sup>14</sup>), Potoff,<sup>18,19</sup> AUA4,<sup>16,46</sup> and TAMie<sup>20,21</sup> force fields. The “short/long” Potoff CH and C parameters are included in parentheses. The ethane specific parameters for TAMie are included in parentheses.

	TraPPE (TraPPE-2)			Potoff (S/L)		
United-atom	$\epsilon/k_B$ (K)	$\sigma$ (nm)	$\lambda$	$\epsilon/k_B$ (K)	$\sigma$ (nm)	$\lambda$
CH <sub>3</sub>	98 (134.5)	0.375 (0.352)	12	121.25	0.3783	16
CH <sub>2</sub>	46	0.395	12	61	0.399	16
CH	10	0.468	12	15 (15/14)	0.46 (0.47/0.47)	16
C	0.5	0.640	12	1.2 (1.45/1.2)	0.61 (0.61/0.62)	16
	AUA4			TAMie		
CH <sub>3</sub>	120.15	0.3607	12	136.318 (130.780)	0.36034 (0.36463)	14
CH <sub>2</sub>	86.29	0.3461	12	52.9133	0.40400	14
CH	50.98	0.3363	12	14.5392	0.43656	14
C	15.04	0.244	12	–	–	–

TABLE V. Non-bonded (intermolecular) parameters for Errington Exp-6 force field.<sup>15</sup>

United-atom	$\epsilon/k_B$ (K)	$\sigma$ (nm)	$\alpha$	$r_{\min}$ (nm)	$r_{\max}$ (nm)
CH <sub>3</sub>	129.6	0.3679	16	0.4094	0.0574
CH <sub>2</sub>	73.5	0.400	22	0.436	0.0221

(as recommended in Reference 15):

$$\epsilon_{ij} = \sqrt{\epsilon_{ii}\epsilon_{jj}} \quad (5)$$

$$\sigma_{ij} = \frac{\sigma_{ii} + \sigma_{jj}}{2} \quad (6)$$

$$\lambda_{ij} = \frac{\lambda_{ii} + \lambda_{jj}}{2} \quad (7)$$

$$\alpha_{ij} = \sqrt{\alpha_{ii}\alpha_{jj}} \quad (8)$$

where the  $ij$  subscript refers to cross-interactions and the subscripts  $ii$  and  $jj$  refer to same-site interactions.

### III. CASE STUDY

The purpose of this case study is to demonstrate that the existing UA and AUA force fields for normal and branched alkanes that were parameterized with VLE properties do not predict the proper  $P\rho T$  behavior at higher temperatures and pressures (with the exception of ethane for the TraPPE-2 potential). Figures 4–5 plot the compressibility factor with respect to inverse temperature for  $n$ -alkanes and branched alkanes, respectively. Note that saturation corresponds to  $Z \approx 0$  for each isochore. The “Potoff” results in Figure 5 are only for the “short/long” model, since the “short/long” model is more accurate than the “generalized” model (available in Section SI.II of Supporting Information).

Note that Figures 4–5 include a constant 1 % uncertainty in the REFPROP correlations for all compounds at all state points. This is a conservative estimate as the reported REFPROP uncertainty for  $\rho$  is typically only 1 % at  $T^{\text{IT}}$  while it decreases near  $T^{\text{sat}}$  to a value  $\leq 0.2$  %. Furthermore, only ethane,<sup>33</sup>  $n$ -butane,<sup>35</sup> isohexane,<sup>37</sup> and neopentane<sup>37</sup> have a reported uncertainty of 1 % at  $T^{\text{IT}}$ . REFPROP uncertainties for propane,<sup>34</sup> isobutane,<sup>35</sup> and  $n$ -octane<sup>36</sup> are actually 0.1 %, 0.4 %, and 0.5 %, respectively, while isooctane<sup>37</sup> does not have a reported uncertainty.

Figure 4 demonstrates that the existing literature force fields for  $n$ -alkanes, while accurate for VLE ( $Z \approx 0$ ), do not capture the correct  $P\rho T$  behavior at high pressures ( $P^{\text{high}}$ ), i.e.  $Z$  at the higher temperatures ( $T > T^{\text{sat}}$ ) and highest isochore densities ( $\rho_3^{\text{IC}}$  and  $\rho_4^{\text{IC}}$ ). Figure 5 shows the same erroneous trend in  $Z$  for branched alkanes. Note that the error in  $Z$  at high temperatures is less obvious because these force fields are typically not as reliable at predicting VLE for branched alkanes as for  $n$ -alkanes, i.e. notice the large deviations at  $Z \approx 0$ . However, it is clear in both Figures 4–5 that none of the force fields adequately reproduces  $Z$  over the entire temperature range, or the slope of  $Z$  with respect to inverse  $T$ .

A surprising trend is that the Errington (AUA Exp-6) model has a positive bias at high

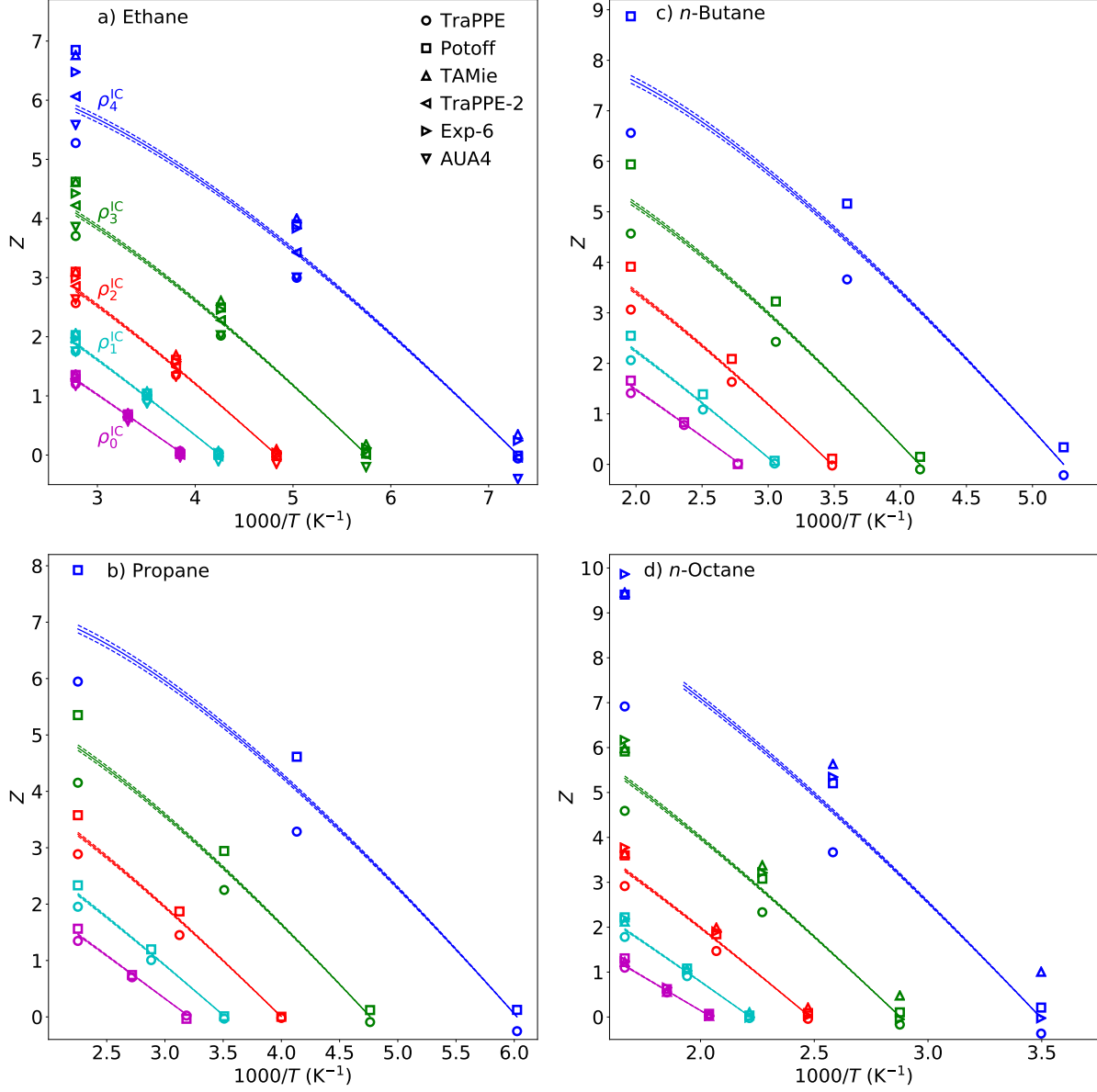


FIG. 4. Compressibility factors ( $Z$ ) along isochores for  $n$ -alkanes. Most force fields are accurate at saturation ( $Z \approx 0$ ) but deviate strongly at higher pressures. Different symbol shapes correspond to the various force fields, with legend in Panel a). Densities are distinguished by color, increase vertically, and are labeled such that  $\rho_0^{\text{IC}} < \rho_1^{\text{IC}} < \rho_2^{\text{IC}} < \rho_3^{\text{IC}} < \rho_4^{\text{IC}}$ . Panels a) to d) correspond to ethane, propane,  $n$ -butane, and  $n$ -octane, respectively. Solid lines represent REFPROP correlations, with dashed lines representing a 1 % uncertainty in REFPROP values.<sup>1,33–36</sup> Simulation error bars computed with block averaging are approximately one symbol size.

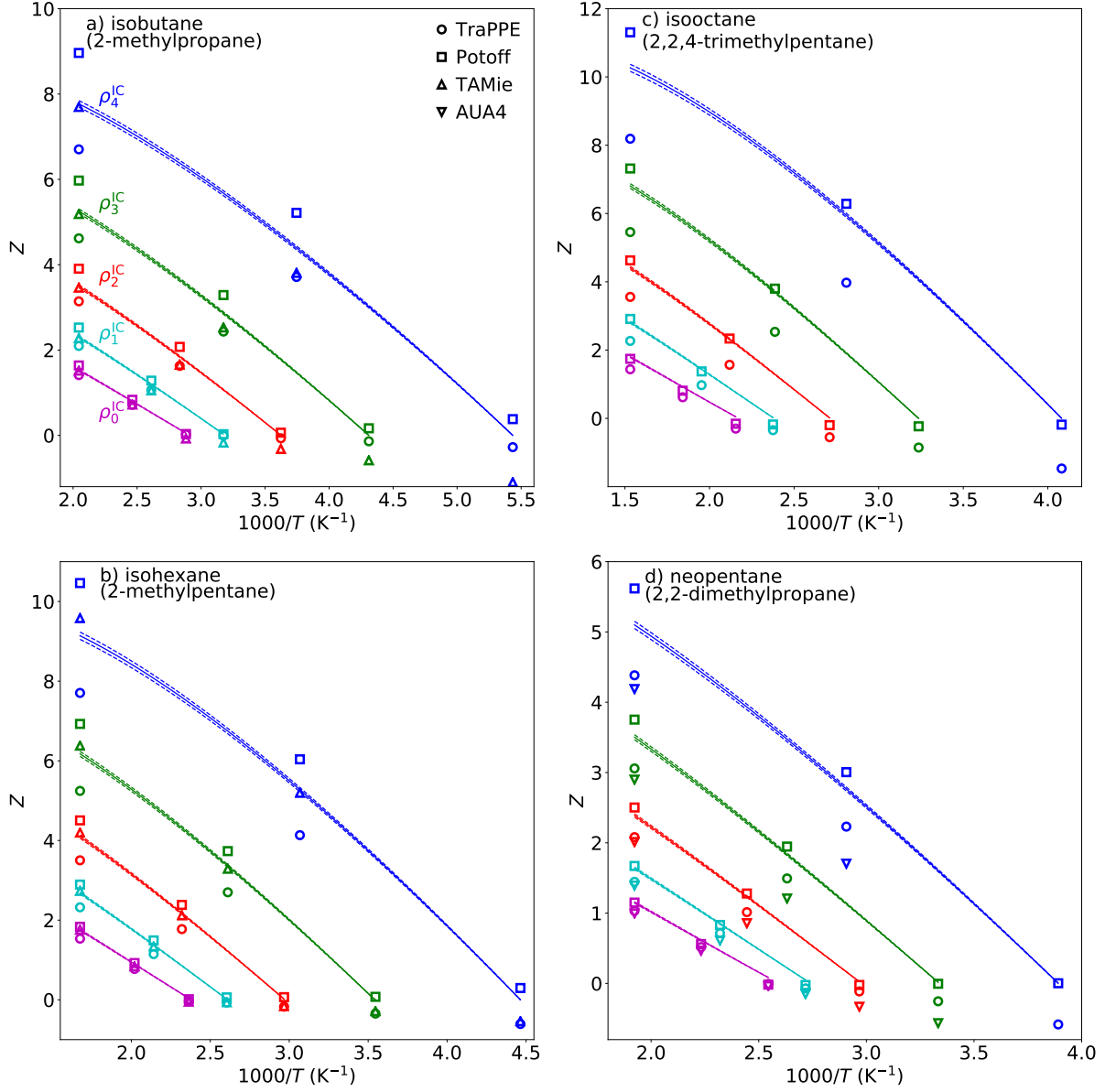


FIG. 5. Compressibility factors ( $Z$ ) along isochores for branched alkanes. Force fields are not as accurate as normal alkanes at saturation ( $Z \approx 0$ ) and deviate strongly at higher pressures. Panels a) to d) correspond to isobutane, isohexane, isooctane, and neopentane, respectively. Symbols, lines, uncertainties, and formatting are the same as those in Figure 4. The Potoff results for isobutane and neopentane use the “short” parameters, while isohexane and isooctane use the “long” parameters (see Table IV).<sup>19</sup>



pressures. This appears to suggest that the repulsive barrier is too steep, despite the fact that the Exp-6 model is typically considered softer than the LJ 12-6. However, the Exp-6 is less repulsive than the LJ 12-6 only at very short distances, e.g.  $r < 0.7r_{\min}$  for  $\alpha = 16$  and  $r < 0.3r_{\min}$  for  $\alpha = 22$ , while it is actually somewhat more repulsive for the closest-range distances sampled in molecular dynamics at these conditions, i.e.  $0.7r_{\min} < r < r_{\min}$  (see inset of Panel b) in Figure 3). More definitive and straight-forward conclusions regarding the shape of the Mie  $\lambda$ -6 repulsive barrier are possible by directly comparing different values of  $\lambda$ .

In general, clear systematic biases are observed for the LJ 12-6 potentials and the Mie  $\lambda$ -6 potentials. Specifically, the LJ 12-6 (TraPPE-UA and AUA4) and Mie  $\lambda$ -6 (Potoff and TAMie) potentials under- and over-predict  $Z$  at high pressures, respectively. These results are intuitive as the repulsive barriers are steeper for the respective Mie 16-6 and 14-6 potentials of the Potoff and TAMie force fields.

The one exception to this trend is the TraPPE-2 model for ethane, which has the most accurate prediction of the entire  $P\rho T$  phase space simulated. Specifically, TraPPE-2 reproduces the REFPROP  $Z$  to within 1 % for all state points except at  $P^{\text{high}}$ , where the average percent deviation (AD%) relative to the REFPROP correlations is still only 3 %.

The performance of TraPPE-2 is somewhat surprising considering that this force field has only three fitting parameters ( $\epsilon$ ,  $\sigma$ , and the effective bond-length) while the TAMie model has these three parameters and an additional fitting parameter ( $\lambda$ ). It is possible that a four parameter optimization, such as that used by TAMie, is overfit to the VLE data and would perform better if high pressure  $P\rho T$  data were included in the parameterization. Furthermore, it is important to note that TraPPE-2 uses a much longer effective bond-length of 0.230 nm while TAMie did not consider bond-lengths larger than 0.194 nm. Therefore, the fact that the TraPPE-2 force field extrapolates to high pressures better than TAMie suggests that, at high pressures, it is important to account for hydrogens with a longer effective bond-length than that typically used for AUA models (see Table I).

Unfortunately, a direct comparison of the non-bonded interactions for AUA force fields is difficult because each model has a different anisotropic displacement, i.e. effective bond-length. By contrast, comparing TraPPE-UA and Potoff is straightforward because

they use the same bond-lengths and the same non-bonded Mie  $\lambda$ -6 potential (Equation 1). For example, since the TraPPE-UA (LJ 12-6) potential under-predicts  $Z$  and the Potoff (UA Mie 16-6) potential over-predicts  $Z$ , it seems reasonable that a UA Mie 13-6, 14-6, or 15-6 model could demonstrate the proper trend.

To investigate this hypothesis, the remainder of this document focuses on the UA Mie  $\lambda$ -6 potential, where all bond-lengths are 0.154 nm to be consistent with the TraPPE and Potoff UA models. Specifically, we perform a Bayesian uncertainty quantification analysis to determine if there exists a set of  $\epsilon$ ,  $\sigma$ , and  $\lambda$  that reasonably predicts  $\rho_1^{\text{sat}}$ ,  $P_v^{\text{sat}}$ , and  $P^{\text{high}}$ . The results in Section V demonstrate that the optimal value of  $\lambda$  for predicting  $P\rho T$  of supercritical fluids and compressed liquids is not capable of predicting VLE properties accurately, and vice-versa.

#### IV. UNCERTAINTY QUANTIFICATION

The results presented in Section III demonstrate that none of the literature UA or AUA force fields, parameterized with VLE data, can reproduce the  $P\rho T$  behavior for supercritical fluids and compressed liquids. However, there is uncertainty in the non-bonded parameters inherited from the VLE data. Therefore, by considering the inherent uncertainty, it is possible that a feasible parameter set exists that adequately predicts VLE and  $P^{\text{high}}$ . By contrast, if none of the  $\epsilon$ ,  $\sigma$ , and  $\lambda$  sets is capable of simultaneously predicting VLE properties and  $Z$  at high pressures, we can conclude that the UA Mie  $\lambda$ -6 potential (and Lennard-Jones 12-6 as a special case) is inadequate for this purpose and, therefore, should not be used when developing FEOS with molecular simulation results.

Bayesian inference is a rigorous approach to determine all feasible  $\epsilon$ ,  $\sigma$ , and  $\lambda$  parameter sets. We refer the reader to the literature for a thorough discussion of Bayesian statistics.<sup>31,47–50</sup> In Section IV A, we review some basic concepts of Bayes’ theorem, define the posterior, likelihood, and prior distributions, and discuss the Markov Chain Monte Carlo (MCMC) approach for sampling from the posterior joint distribution of the parameters. MCMC can be computationally burdensome, especially when molecular simulation is required to compute the likelihood. For this reason, we utilize surrogate models

to reduce the computational cost of MCMC by several orders of magnitude. Section IV B demonstrates how these surrogate models estimate  $\rho_1^{\text{sat}}$ ,  $P_v^{\text{sat}}$ , and  $Z$  for a given set of  $\epsilon$ ,  $\sigma$ , and  $\lambda$ . We implement this analysis for  $n$ -alkanes to generate joint distributions of  $\epsilon_{\text{CH}_3}-\sigma_{\text{CH}_3}$  and  $\epsilon_{\text{CH}_2}-\sigma_{\text{CH}_2}$  for different values of  $\lambda_{\text{CH}_3}$  and  $\lambda_{\text{CH}_2}$ , respectively.

## A. Bayesian Inference

### 1. Theory

Bayes' theorem states

$$Pr(\theta|D, M) = \frac{Pr(D|\theta, M)Pr(\theta|M)}{Pr(D|M)} \quad (9)$$

where  $Pr$  denotes a probability distribution function,  $\theta$  is the parameter set,  $M$  is the model, and  $D$  are the data.  $Pr(\theta|D, M)$  is commonly referred to as the “posterior”,  $Pr(D|\theta, M)$  is the “likelihood” (alternatively expressed as  $L(\theta|D, M)$ ),  $Pr(\theta|M)$  is the “prior”, and  $Pr(D|M)$  is a normalization constant which is also the “model evidence”.

The “model evidence” is used in model selection, by computing the probability of different models given the data:

$$Pr(M|D) = \frac{Pr(D|M)Pr(M)}{Pr(D)} \quad (10)$$

where  $Pr(M)$  is the “model prior”,  $Pr(D)$  is a normalization constant, and  $Pr(M|D)$  is the “model posterior”. The ratio of  $Pr(M|D)$  between two different models ( $M_i$  and  $M_j$ ), known as the Bayes factor ( $K_{ij}$ ), provides the relative probability of models  $M_i$  and  $M_j$ , given the data  $D$ .

The parameter uncertainty propagates when estimating another quantity of interest ( $QoI$ ), which may or may not be included in  $D$ , according to:<sup>31</sup>

$$Pr(QoI|D, M) = \int Pr(QoI|\theta, M)Pr(\theta|D, M)d\theta \quad (11)$$

This expression is commonly referred to as “robust posterior prediction.” Note that the uncertainty in  $QoI$ , obtained from  $Pr(QoI|D, M)$ , does not account for deficiencies in the model itself, only the uncertainty in the model parameters.

## 2. Application

Bayesian inference is used to quantify the uncertainty in the non-bonded parameters ( $\epsilon$  and  $\sigma$ ) and to determine the evidence for different values of  $\lambda$  based on VLE data. For clarity, we rewrite Equations 9-10 for the specific case studied by substituting  $\epsilon$  and  $\sigma$  for  $\theta$ ,  $\lambda$  for  $M$ , and  $\rho_1^{\text{sat}}$  and  $P_v^{\text{sat}}$  for  $D$ :

$$Pr(\epsilon, \sigma | \rho_1^{\text{sat}}, P_v^{\text{sat}}, \lambda) = \frac{L(\epsilon, \sigma | \rho_1^{\text{sat}}, P_v^{\text{sat}}, \lambda) Pr(\epsilon, \sigma | \lambda)}{Pr(\rho_1^{\text{sat}}, P_v^{\text{sat}} | \lambda)} \quad (12)$$

$$Pr(\lambda | \rho_1^{\text{sat}}, P_v^{\text{sat}}) = \frac{Pr(\rho_1^{\text{sat}}, P_v^{\text{sat}} | \lambda) Pr(\lambda)}{Pr(\rho_1^{\text{sat}}, P_v^{\text{sat}})} \quad (13)$$

where in this context  $\rho_1^{\text{sat}}$  and  $P_v^{\text{sat}}$  are arrays of experimental data values. Note that  $\theta$  does not include  $\lambda$ , since we use  $\lambda$  to distinguish between models. The “model evidence”,  $Pr(\rho_1^{\text{sat}}, P_v^{\text{sat}} | \lambda)$  in Equation 13, for different values of  $\lambda$  is determined by integrating the numerator of Equation 12 for all values of  $\epsilon$  and  $\sigma$ .

To compute the Bayes factor between two values of  $\lambda$  (i.e. between different models,  $M_i$  and  $M_j$ ), we assume that the prior evidence is equal for all positive values of  $\epsilon$ ,  $\sigma$ , and  $\lambda$  (within a feasible range). Specifically, we use bounded uniform prior distributions for  $Pr(\epsilon, \sigma | \lambda)$  in Equation 12 and  $Pr(\lambda)$  in Equation 13, where the lower bound is 0 and the upper bound is an order of magnitude greater than the literature values for  $\epsilon$ ,  $\sigma$ , and  $\lambda$ . Due to the large amount of information contained in the data,  $D$ , the use of a uniform prior does not impact our results, i.e. the data “overwhelms” the prior. One advantage of using a uniform prior is that the Bayes factor,  $K_{ij}$ , depends completely on the likelihood:

$$K_{ij} = \frac{Pr(\lambda_j | \rho_1^{\text{sat}}, P_v^{\text{sat}})}{Pr(\lambda_i | \rho_1^{\text{sat}}, P_v^{\text{sat}})} = \frac{\int L(\epsilon, \sigma | \rho_1^{\text{sat}}, P_v^{\text{sat}}, \lambda_j) d\epsilon d\sigma}{\int L(\epsilon, \sigma | \rho_1^{\text{sat}}, P_v^{\text{sat}}, \lambda_i) d\epsilon d\sigma} \quad (14)$$

where  $\lambda_i$  and  $\lambda_j$  are the different (fixed) values of  $\lambda$  being compared.

We utilize robust posterior prediction (Equation 11) to propagate the joint parameter uncertainty in  $\epsilon$  and  $\sigma$  (for a given  $\lambda$ ) to three different  $QoI$ , specifically,  $\rho_1^{\text{sat}}$ ,  $P_v^{\text{sat}}$ , and  $Z$ . For example, the uncertainty in predicting  $Z$  is obtained from:

$$Pr(Z | \rho_1^{\text{sat}}, P_v^{\text{sat}}, \lambda) = \int Pr(Z | \epsilon, \sigma, \lambda) Pr(\epsilon, \sigma | \rho_1^{\text{sat}}, P_v^{\text{sat}}, \lambda) d\epsilon d\sigma \quad (15)$$

Similar expressions exist for  $Pr(\rho_1^{\text{sat}}|\rho_1^{\text{sat}}, P_v^{\text{sat}}, \lambda)$  and  $Pr(P_v^{\text{sat}}|\rho_1^{\text{sat}}, P_v^{\text{sat}}, \lambda)$ , where posterior prediction allows for uncertainty estimates in  $\rho_1^{\text{sat}}$  and  $P_v^{\text{sat}}$  at any temperature, not just those included in  $D$ .

### 3. Implementation

Markov Chain Monte Carlo (MCMC) is the traditional approach for numerically sampling from the probability distribution  $Pr(\epsilon, \sigma|\rho_1^{\text{sat}}, P_v^{\text{sat}}, \lambda)$ . We use the Metropolis-Hastings algorithm to create a Markov Chain by proposing new  $\epsilon$  and  $\sigma$  sets and accepting those moves based on the criterion:

$$\alpha = \min \left( 1, \frac{Pr(\epsilon_{i+1}, \sigma_{i+1}|\rho_1^{\text{sat}}, P_v^{\text{sat}}, \lambda)Q(\epsilon_i, \sigma_i|\epsilon_{i+1}, \sigma_{i+1}, s_\epsilon^2, s_\sigma^2)}{Pr(\epsilon_i, \sigma_i|\rho_1^{\text{sat}}, P_v^{\text{sat}}, \lambda)Q(\epsilon_{i+1}, \sigma_{i+1}|\epsilon_i, \sigma_i, s_\epsilon^2, s_\sigma^2)} \right) \quad (16)$$

where  $\alpha$  is the acceptance probability,  $\epsilon_i$  and  $\sigma_i$  are the previous parameter set,  $\epsilon_{i+1}$  and  $\sigma_{i+1}$  are the proposed parameter set, and  $Q$  is the proposal distribution from which  $\epsilon_{i+1}$  and  $\sigma_{i+1}$  are sampled. In this study,  $Q$  is a bi-variate normal distribution with mean equal to  $\epsilon_i$  and  $\sigma_i$ , variance of  $s_\epsilon^2$  and  $s_\sigma^2$ , and a covariance of 0.

The amount to which  $\epsilon$  or  $\sigma$  is varied for each MCMC step (the difference between  $\epsilon_{i+1}$  and  $\epsilon_i$  or between  $\sigma_{i+1}$  and  $\sigma_i$ ) depends on  $Q$ , specifically, on  $s_\epsilon^2$  and  $s_\sigma^2$ . These parameters ( $s_\epsilon^2$  and  $s_\sigma^2$ ) are tuned such that approximately  $\frac{1}{3}$  of the moves are accepted, i.e.  $s_\epsilon^2$  and  $s_\sigma^2$  are decreased if the acceptance rate of MCMC moves is less than  $\frac{1}{3}$ , and vice-versa. This “tuning” period (also referred to as a “burn-in” period) is followed by a production period where  $s_\epsilon^2$  and  $s_\sigma^2$  do not change.

Since  $\epsilon_{i+1}$  and  $\sigma_{i+1}$  are highly correlated with  $\epsilon_i$  and  $\sigma_i$ , it is important to “thin” the MCMC  $\epsilon$  and  $\sigma$  parameter sets ( $\epsilon_{\text{MCMC}}$  and  $\sigma_{\text{MCMC}}$ ), i.e. every  $j^{\text{th}}$  parameter set is stored. Section [SI.III](#) of Supporting Information provides an MCMC example with some details (i.e. number of steps for burn-in and production, frequency that  $s_\epsilon^2$  and  $s_\sigma^2$  are updated, resulting acceptance rates, etc.).

The joint distribution of the parameter sets sampled from MCMC ( $\theta_{\text{MCMC}}$ , or specifically,  $\epsilon_{\text{MCMC}}$  and  $\sigma_{\text{MCMC}}$ ) quantifies the uncertainty in  $\epsilon$  and  $\sigma$  (see Figure 7 and 12 in Section V). The integration required for robust posterior prediction (see Equations 11 and 15)

is approximated from the distribution of  $QoI$  values evaluated for each MCMC parameter set, i.e.  $QoI(\theta_{\text{MCMC}}|D, M)$  or the more succinct notation  $QoI_{\text{MCMC}}$ . From  $QoI_{\text{MCMC}}$ , standard statistical methods are used to approximate the  $QoI$  uncertainty at a desired credible level. For example, the histograms and uncertainties reported in Section V are obtained from distributions of  $\rho_{\text{l,MCMC}}^{\text{sat}}$ ,  $P_{\text{v,MCMC}}^{\text{sat}}$ , and  $Z_{\text{MCMC}}$ .

Because MCMC moves are accepted based on Equation 16 and the denominator in Equation 12 (i.e.  $Pr(\rho_1^{\text{sat}}, P_v^{\text{sat}}|\lambda)$ ) does not depend on  $\epsilon$  and  $\sigma$ , the acceptance probability is independent of  $Pr(\rho_1^{\text{sat}}, P_v^{\text{sat}}|\lambda)$ . Also, as mentioned previously, we use a weakly informative uniform prior over a larger than feasible range of parameters such that the acceptance probability is independent of  $Pr(\epsilon, \sigma|\lambda)$ . Furthermore,  $Q$  is chosen to be symmetric such that the  $Q$  terms in the numerator and denominator of Equation 16 cancel. Therefore, the probability of accepting  $\epsilon_{i+1}$  and  $\sigma_{i+1}$  is based completely on the likelihood:

$$\alpha = \min \left( 1, \frac{L(\epsilon_{i+1}, \sigma_{i+1}|\rho_1^{\text{sat}}, P_v^{\text{sat}}, \lambda)}{L(\epsilon_i, \sigma_i|\rho_1^{\text{sat}}, P_v^{\text{sat}}, \lambda)} \right) \quad (17)$$

The likelihood,  $L(\epsilon, \sigma, |\rho_1^{\text{sat}}, P_v^{\text{sat}}, \lambda)$ , is calculated from a normal distribution:

$$L(\epsilon, \sigma, |\rho_1^{\text{sat}}, P_v^{\text{sat}}, \lambda) = \prod_k \frac{1}{\sqrt{2\pi s_{\text{D,SM}}^2(T_k^{\text{sat}})}} \exp \left( -\frac{(\rho_{\text{l,SM}}^{\text{sat}}(\epsilon, \sigma, \lambda; T_k^{\text{sat}}) - \rho_{\text{l,k}}^{\text{sat}})^2}{2s_{\text{D,SM}}^2(T_k^{\text{sat}})} \right) \prod_k \frac{1}{\sqrt{2\pi s_{\text{D,SM}}^2(T_k^{\text{sat}})}} \exp \left( -\frac{(P_{\text{v,SM}}^{\text{sat}}(\epsilon, \sigma, \lambda; T_k^{\text{sat}}) - P_{\text{v,k}}^{\text{sat}})^2}{2s_{\text{D,SM}}^2(T_k^{\text{sat}})} \right) \quad (18)$$

where the first and second products are over the experimental  $\rho_1^{\text{sat}}$  and  $P_v^{\text{sat}}$  data, respectively,  $T_k^{\text{sat}}$  is the saturation temperature that corresponds the  $k^{\text{th}}$  data point, “SM” refers to the surrogate model (see Section IV B) used to estimate  $\rho_1^{\text{sat}}$  or  $P_v^{\text{sat}}$  for a given  $\epsilon, \sigma, \lambda$ , and  $T^{\text{sat}}$ , and  $s_{\text{D,SM}}^2$  is the combined variance of the experimental data and the surrogate model. The variances are independent, meaning that the combined variance is the sum of the experimental and surrogate model variances, i.e.  $s_{\text{D,SM}}^2 = s_{\text{D}}^2 + s_{\text{SM}}^2$ .<sup>48</sup>

## B. Surrogate Model

A typical Markov Chain requires  $O(10^4 \text{ to } 10^5)$  Monte Carlo steps, where the likelihood function must be evaluated at each step. Since  $L(\theta|D, M)$  depends on the force

field parameters ( $\epsilon$ ,  $\sigma$ , and  $\lambda$ ), an MCMC approach is computationally infeasible if computing  $L(\theta|D, M)$  requires performing direct molecular simulations for every proposed parameter set. Furthermore, propagation of uncertainty with robust posterior prediction may require  $O(10^2 \text{ to } 10^3)$   $\theta_{\text{MCMC}}$  parameter sets for adequate representations of  $Pr(QoI|D, M)$  (see Equations 11 and 15). For these reasons, surrogate models to estimate  $\rho_{\text{l,MCMC}}^{\text{sat}}$ ,  $P_{\text{v,MCMC}}^{\text{sat}}$  and  $Z_{\text{MCMC}}$  are essential for this study.

### 1. Multistate Bennett Acceptance Ratio

We use a configuration-sampling-based surrogate model, where configurations are sampled using a small group of reference parameter sets ( $\theta_{\text{ref}}$ , consisting of  $\epsilon_{\text{ref}}$ ,  $\sigma_{\text{ref}}$ , and  $\lambda_{\text{ref}}$ ).<sup>44</sup> Specifically,  $NVT$  ensemble averages for the MCMC parameter sets ( $\theta_{\text{MCMC}}$ ) are estimated by reweighting the sampled reference configurations using Multistate Bennett Acceptance Ratio (MBAR).<sup>51</sup> MBAR is a nearly exact surrogate model when a sufficient number of configurations sampled by  $\theta_{\text{ref}}$  are similar to those that would be sampled with direct simulation of  $\theta$ , which can be easily verified by statistical measures (see discussion on number of effective samples in Reference 44). For this purpose, we use a single value of  $\epsilon_{\text{ref}}$  with nine evenly spaced  $\sigma_{\text{ref}}$  values for each fixed value of  $\lambda_{\text{ref}} = \lambda$ .<sup>44</sup>

### 2. Isothermal isochoric integration

The properties that are estimated using MBAR are the departure internal energy ( $U^{\text{dep}} \equiv U - U^{\text{ig}}$ , where  $U^{\text{ig}}$  is the ideal gas internal energy) and the compressibility factor ( $Z \equiv \frac{P}{\rho R_g T}$ , where  $R_g$  is the universal gas constant). Isothermal isochoric integration (ITIC) converts the MBAR estimated  $U^{\text{dep}}$  and  $Z$  values at the 19 ITIC state points to saturation temperatures ( $T^{\text{sat}}$ ), saturated liquid densities ( $\rho_{\text{l}}^{\text{sat}}$ ), saturated vapor densities ( $\rho_{\text{v}}^{\text{sat}}$ ), and saturated vapor pressures ( $P_{\text{v}}^{\text{sat}}$ ). This is important since  $\rho_{\text{l}}^{\text{sat}}$  and  $P_{\text{v}}^{\text{sat}}$  are the data ( $D$ ) included in  $L(\theta|D)$ . Details for the combined implementation of MBAR and ITIC (MBAR-ITIC) is discussed elsewhere.<sup>44</sup>

The ITIC equations are:

$$\frac{A^{\text{dep}}}{R_g T^{\text{sat}}} = \int_0^{\rho^{\text{IC}}} \frac{Z-1}{\rho} d\rho|_{T=T^{\text{IT}}} + \int_{T^{\text{IT}}}^{T^{\text{sat}}} U^{\text{dep}} d\left(\frac{1}{R_g T}\right)|_{\rho=\rho^{\text{IC}}} \quad (19)$$

$$\rho_v^{\text{sat}} \approx \rho_l^{\text{sat}} \exp\left(\frac{A^{\text{dep}}}{R_g T^{\text{sat}}} + Z_l^{\text{sat}} - 1 - 2B_2 \rho_v^{\text{sat}} - 1.5B_3 (\rho_v^{\text{sat}})^2\right) \quad (20)$$

$$P_v^{\text{sat}} \approx (1 + B_2 \rho_v^{\text{sat}} + B_3 (\rho_v^{\text{sat}})^2) \rho_v^{\text{sat}} R_g T^{\text{sat}} \quad (21)$$

$$Z_l^{\text{sat}} = \frac{P_v^{\text{sat}}}{\rho_l^{\text{sat}} R_g T^{\text{sat}}} \quad (22)$$

where  $A^{\text{dep}} \equiv A - A^{\text{ig}}$  is the Helmholtz free energy departure from ideal gas for  $T = T^{\text{sat}}$  and  $\rho = \rho^{\text{IC}} = \rho_l^{\text{sat}}$ ,  $Z_l^{\text{sat}}$  is the saturated liquid compressibility factor,  $B_2$  is the second virial coefficient,  $B_3$  is the third virial coefficient,  $T^{\text{IT}}$  is the isothermal temperature, and  $\rho^{\text{IC}}$  is the isochoric density. For details regarding the implementation of ITIC, see References 43–45. As discussed in our previous work,<sup>44</sup> the  $B_2$  and  $B_3$  values found in Equations 20-21 are calculated using REFPROP correlations.<sup>1</sup> The use of REFPROP correlations introduces a small bias in the resulting  $\rho_l^{\text{sat}}$  and  $P_v^{\text{sat}}$ , which is accounted for in the surrogate model uncertainty.

The ITIC analysis provides VLE properties at only 5 saturation temperature values ( $T_{\text{ITIC}}^{\text{sat}}$ ), while the experimental data set may have hundreds of saturation temperatures ( $T_D^{\text{sat}}$ ). Although it is possible to use computed values from an empirical correlation fit to experimental data (i.e. REFPROP, ThermoData Engine (TDE)) as the data set, it is considered best practice for Bayesian inference that  $D$  consist of raw experimental data. For this reason, we instead use empirical model fits to interpolate the ITIC VLE properties ( $T_{\text{ITIC}}^{\text{sat}}$ ,  $\rho_{l,\text{ITIC}}^{\text{sat}}$ , and  $P_{v,\text{ITIC}}^{\text{sat}}$ ) so that  $\rho_l^{\text{sat}}$  and  $P_v^{\text{sat}}$  can be estimated at any value of  $T^{\text{sat}}$ . Specifically, we fit  $P_{v,\text{ITIC}}^{\text{sat}}$  and  $T_{\text{ITIC}}^{\text{sat}}$  to the Antoine equation:

$$\log_{10}(P_v^{\text{sat}}) = a_0 + \frac{a_1}{T^{\text{sat}} + a_2} \quad (23)$$

where  $a_i$  are fitting parameters. We fit  $\rho_{l,\text{ITIC}}^{\text{sat}}$  and  $T_{\text{ITIC}}^{\text{sat}}$  to a combined rectilinear and density scaling law expression:<sup>24</sup>

$$\rho_l^{\text{sat}} = b_0 + b_1(b_2 - T^{\text{sat}}) + b_3(b_2 - T^{\text{sat}})^\beta \quad (24)$$



where  $b_i$  are fitting parameters, and  $\beta = 0.326$ .  $b_0$  and  $b_2$  only provide rough estimates of the critical density ( $\rho_c$ ) and critical temperature ( $T_c$ ). More reliable estimates of the critical point require simultaneous fitting of  $\rho_{v,ITIC}^{\text{sat}}$  to a similar expression, but this is unnecessary for our purposes since  $D$  does not include the critical constants. Note that Equations 23-24 are only used to interpolate ITIC values, and not to extrapolate to higher or lower  $T^{\text{sat}}$ . These equations are reliable over the limited temperature range studied ( $0.45 < T_r < 0.85$ ), whereas a wider temperature range would require more flexible models.<sup>52,53</sup>

In summary, MBAR, ITIC, and Equations 23-24 enable prediction of  $\rho_1^{\text{sat}}$  and  $P_v^{\text{sat}}$  over a range of  $T^{\text{sat}}$  for any  $\epsilon$ ,  $\sigma$ , and  $\lambda$  by performing a small number of direct  $NVT$  simulations with only a few reference parameter sets. The non-bonded energies and forces, which are required for MBAR and ITIC, are rapidly recomputed post-simulation with  $\theta_{\text{MCMC}}$  for each reference configuration (for details on so-called “basis functions” see Reference 54 and Section SI.IV of Supporting Information in Reference 44). In total, this methodology reduces the computational cost for computing  $L(\theta|D)$  by several orders of magnitude compared to direct simulation of VLE, using Gibbs Ensemble Monte Carlo (GEMC) or Grand Canonical Monte Carlo (GCMC) histogram reweighting (HR).

### 3. *Uncertainty model*

Quantifying the surrogate model variance ( $s_{\text{SM}}^2$ ) is essential for evaluating  $L(\theta|D)$ . While only a brief description is provided here, details are found in Section SI.IV of Supporting Information. Rather than performing a rigorous statistical assessment of MBAR, ITIC, and Equations 23-24, we use an empirical approach for estimating  $s_{\text{SM}}^2$ . Specifically, we compute the deviation between the surrogate model estimates of  $\rho_1^{\text{sat}}$  and  $P_v^{\text{sat}}$  for TraPPE-UA and Potoff with those reported in the literature for the respective force fields obtained using Gibbs Ensemble Monte Carlo (GEMC) or Grand Canonical Monte Carlo (GCMC) histogram reweighting (HR).<sup>12,18</sup> Although this is a rough approximation for estimating  $s_{\text{SM}}^2$ , the benefit of this inter-laboratory comparison is that  $s_{\text{SM}}^2$  accounts for “dark uncertainty”,<sup>55</sup> i.e. uncertainties that arise from unknown sources which can lead to unresolvable discrepancies between research groups.<sup>56</sup> These non-statistical uncertainties

are typically associated with different simulation packages, MD instead of MC, finite-size effects, and post-simulation analysis (e.g. ITIC rather than HR).

As shown in Figure 6, the surrogate model uncertainty ( $u_{\text{SM}}$ , reported at the 95 % confidence level) for  $\rho_1^{\text{sat}}$  is 0.3 % up to  $0.75T_c$  and increases linearly to 1.5 % at the maximum  $T^{\text{sat}}$ . The surrogate model uncertainty for  $P_v^{\text{sat}}$  is 20 % at the minimum  $T_{\text{sat}}$  and decreases linearly to 7 % at  $0.6T_c$ , where it remains constant for higher temperatures. Note that these are conservative estimates of  $u_{\text{SM}}$ , where other studies suggest smaller uncertainties in MBAR and ITIC.<sup>43–45</sup> In fact, for the compounds investigated in this study, these uncertainties are much larger than the experimental uncertainties ( $u_{\text{D}}$ , at the 95 % confidence level)<sup>57</sup> and, therefore, the size of the parameter space sampled by MCMC depends almost entirely on  $u_{\text{SM}}$ . The use of a conservative  $u_{\text{SM}}$  model is intentional in this regard, namely, so that the  $\theta_{\text{MCMC}}$  sampled points represent practically all of the feasible  $\epsilon$  and  $\sigma$  parameter sets (for a given  $\lambda$ ) optimized with  $\rho_1^{\text{sat}}$  and  $P_v^{\text{sat}}$ .

## V. RESULTS

In this section, we use MCMC and the aforementioned surrogate models to determine the parameter uncertainty in  $\text{CH}_3$  and  $\text{CH}_2$  interaction sites of  $n$ -alkanes. As the simulation results of branched alkanes are significantly less accurate than those of  $n$ -alkanes for both VLE and high pressure properties (cf. Figures 4 and 5), we do not investigate the uncertainties of CH and C interaction sites.

Since the common practice is to limit  $\lambda$  to integer values (see Section II B), we perform several independent MCMC runs using a single, fixed, integer value of  $\lambda$ . The Bayesian inference analysis for  $\text{CH}_3$  and  $\text{CH}_2$  sites is performed sequentially. Specifically, rather than sampling from a four-dimensional parameter space (i.e.  $\epsilon_{\text{CH}_3}$ ,  $\epsilon_{\text{CH}_2}$ ,  $\sigma_{\text{CH}_3}$ , and  $\sigma_{\text{CH}_2}$  for a given value of  $\lambda_{\text{CH}_3}$  and  $\lambda_{\text{CH}_2}$ ), we implement a pair of two-dimensional MCMC runs by assuming the  $\text{CH}_3$  parameters from ethane are transferable to propane,  $n$ -butane, and  $n$ -octane.

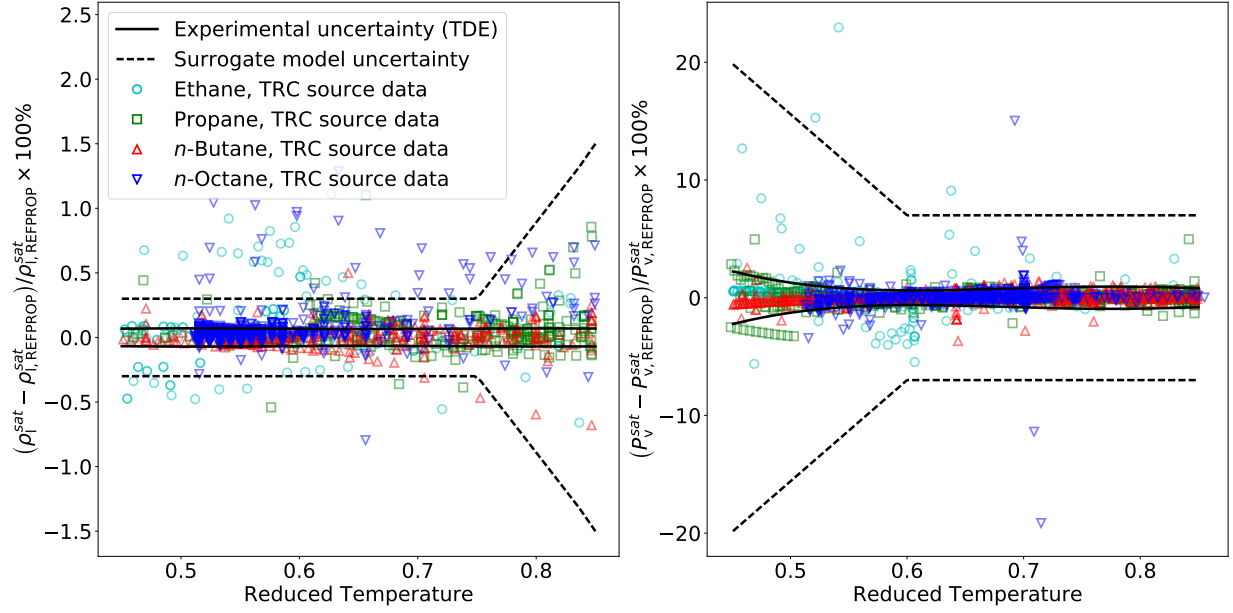


FIG. 6. Uncertainty assessment. Experimental (TDE) uncertainties are negligible compared to surrogate model uncertainties. Panels a) and b) plot the uncertainties for  $\rho_l^{\text{sat}}$  and  $P_v^{\text{sat}}$  with respect to reduced temperature (absolute temperature divided by the REFPROP  $T_c$ ). Uncertainties are computed at the 95 % confidence level using the respective  $s_D^2$  and  $s_{SM}^2$  values. Also included are percent deviations between the REFPROP values<sup>1,33–36</sup> and the experimental data used in Equation 18 to compute the likelihood for ethane, propane, *n*-butane, and *n*-octane (from the Thermodynamics Research Center, TRC, source data).<sup>57</sup>

### A. Ethane

Figures 7-10 present the MCMC results for ethane with  $13 \leq \lambda_{\text{CH}_3} \leq 18$ . Figure 7 demonstrates that the feasible region of  $\epsilon_{\text{CH}_3}$  depends strongly on  $\lambda_{\text{CH}_3}$ , namely, larger values of  $\lambda_{\text{CH}_3}$  require larger values of  $\epsilon_{\text{CH}_3}$ . By contrast, we observe a much smaller shift towards larger values of  $\sigma_{\text{CH}_3}$  with increasing  $\lambda_{\text{CH}_3}$ . This observation is consistent with Reference 18.

Figures 8-9 compare the performance of different values of  $\lambda$  for  $\rho_l^{\text{sat}}$ ,  $P_v^{\text{sat}}$ , and  $Z$ . Notice that the insets in Figure 8 plot the mean absolute percent deviation (MAPD%) to quantify the goodness of fit to VLE data, while the inset in Figure 9 plots the average de-

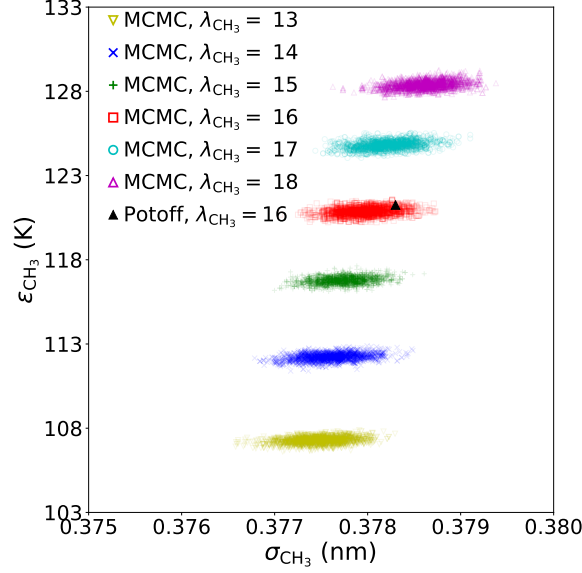


FIG. 7. MCMC sampled parameter sets for different values of  $\lambda_{\text{CH}_3}$  ( $\epsilon_{\text{CH}_3, \text{MCMC}}$  and  $\sigma_{\text{CH}_3, \text{MCMC}}$ ).  $\epsilon_{\text{CH}_3}$  is strongly correlated with  $\lambda_{\text{CH}_3}$  and  $\sigma_{\text{CH}_3}$ , while  $\sigma_{\text{CH}_3}$  and  $\lambda_{\text{CH}_3}$  are only weakly correlated. The Potoff parameter set is included as a reference for  $\lambda_{\text{CH}_3} = 16$ .<sup>18</sup>

viation (AD%) to demonstrate the positive bias in  $P^{\text{high}}$ . Note also that because MAPD% and AD% are percent deviations they are not directly related to the squared deviations of the normal distribution used to compute the likelihood. We plot MAPD% and AD% as these are easier to conceptualize and quantify.

Figure 8 Panel a) with the corresponding inset demonstrates that the best prediction of  $\rho_1^{\text{sat}}$  is obtained for higher values of  $\lambda_{\text{CH}_3}$ . However, while the  $\rho_1^{\text{sat}}$  MAPD% for  $\lambda_{\text{CH}_3} = 15$  to 18 are similar,  $\lambda_{\text{CH}_3} = 13$  and 14 have significantly higher  $\rho_1^{\text{sat}}$  MAPD%. Figure 8 Panel b) demonstrates that  $\lambda_{\text{CH}_3} \leq 14$  and  $\lambda_{\text{CH}_3} \geq 17$  over- and under-predict  $P_v^{\text{sat}}$  at low temperatures, respectively, while  $\lambda_{\text{CH}_3} = 15$  and 16 have the best trend for  $P_v^{\text{sat}}$ . The inset for Panel b) shows that  $\lambda_{\text{CH}_3} = 15$  has the lowest MAPD% in  $P_v^{\text{sat}}$ .

Finally, Figure 9 demonstrates that all of the sampled  $\epsilon_{\text{CH}_3, \text{MCMC}}$  and  $\sigma_{\text{CH}_3, \text{MCMC}}$  parameter sets for  $\lambda_{\text{CH}_3} \geq 14$  over-predict  $Z$  at high temperatures and densities ( $P^{\text{high}}$ ). As expected, the larger the value of  $\lambda_{\text{CH}_3}$ , the more the force field over-predicts  $P^{\text{high}}$ .

While Figures 8-9 plot the results for  $\rho_1^{\text{sat}}$ ,  $P_v^{\text{sat}}$ , and  $Z$  individually, Figure 10 helps to vi-

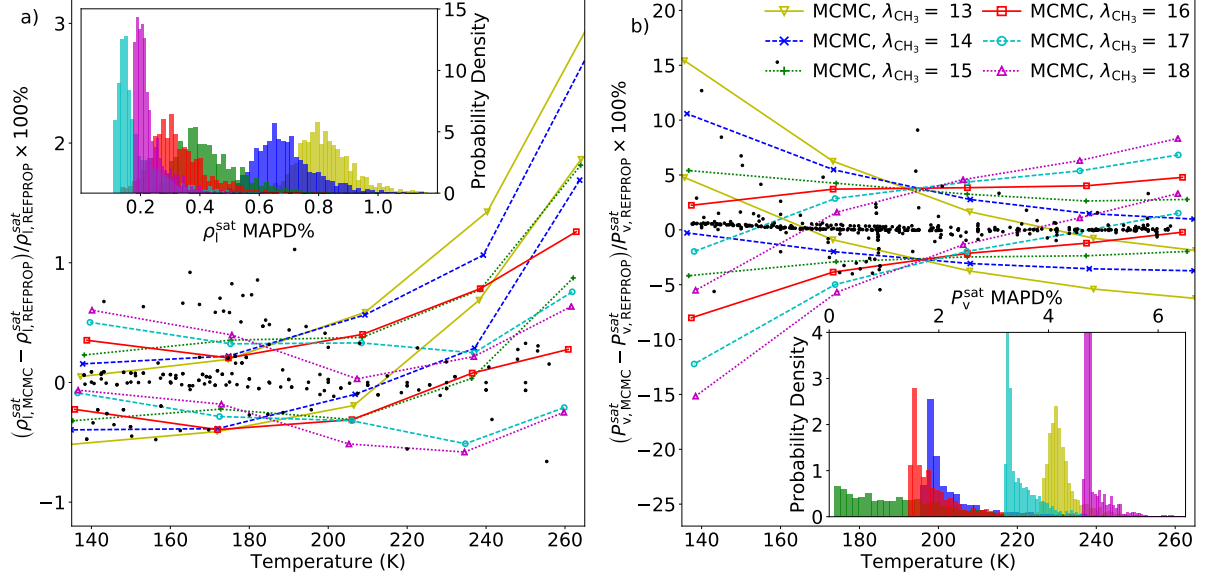


FIG. 8. Ethane VLE properties with respect to temperature for  $\lambda_{\text{CH}_3} = 13$  to 18. Different trends are observed depending on the value of  $\lambda_{\text{CH}_3}$ . Panels a) and b) plot the percent deviation from REFPROP values<sup>1,33</sup> for  $\rho_{l,\text{MCMC}}^{\text{sat}}$  and  $P_{v,\text{MCMC}}^{\text{sat}}$ , respectively. Robust posterior prediction propagates the joint parameter uncertainties from  $\epsilon_{\text{CH}_3}$  and  $\sigma_{\text{CH}_3}$  to  $\rho_l^{\text{sat}}$  and  $P_v^{\text{sat}}$ . The upper and lower lines for each  $\lambda$  correspond to the 95 % credible interval obtained from  $QoI_{\text{MCMC}}$ . Insets of Panels a) and b) are histograms of the MAPD% in  $\rho_{l,\text{MCMC}}^{\text{sat}}$  and  $P_{v,\text{MCMC}}^{\text{sat}}$ , respectively. Experimental data used to compute the likelihood are included as black dots.<sup>57</sup>

visualize the overall performance of different values of  $\lambda_{\text{CH}_3}$  for simultaneously predicting all three quantities of interest. In Panel a), notice the trade-off between the MAPD% of  $\rho_l^{\text{sat}}$  and  $P_v^{\text{sat}}$ . This compromise between two competing properties included in the objective function, namely,  $\rho_l^{\text{sat}}$  and  $P_v^{\text{sat}}$ , is known as a Pareto front.<sup>23,58,59</sup> The optimal location for a Pareto front is the bottom left region of the plot (low MAPD% for both  $\rho_l^{\text{sat}}$  and  $P_v^{\text{sat}}$ ) while the worst location is the top right region (high MAPD% for both  $\rho_l^{\text{sat}}$  and  $P_v^{\text{sat}}$ ). Note that the inset of Panel a) includes an approximate “overall” Pareto front that combines the results for all values of  $\lambda_{\text{CH}_3}$ . Although not depicted for visual clarity, the “L” shaped frontier for different colors/symbols demonstrates that each  $\lambda_{\text{CH}_3}$  value also has its own Pareto front. Because the overall Pareto front consists of points from the  $15 \leq \lambda_{\text{CH}_3} \leq 17$

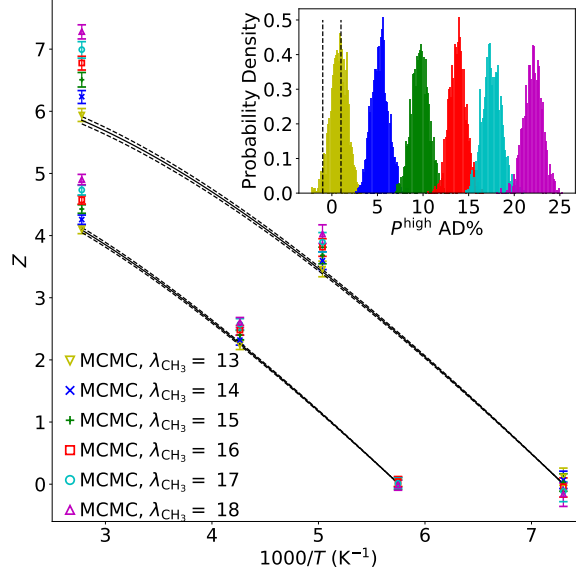


FIG. 9. Ethane isochore results for  $\lambda_{\text{CH}_3} = 13$  to 18. Inadequacies of the UA Mie  $\lambda$ -6 potential are observed in  $Z$  for the two highest isochore densities ( $\rho_3^{\text{IC}}$  and  $\rho_4^{\text{IC}}$ ) by propagating the joint uncertainties in  $\epsilon_{\text{CH}_3}$  and  $\sigma_{\text{CH}_3}$  for different values of  $\lambda_{\text{CH}_3}$ . The inset plots the distribution of average deviation (AD%) in  $P^{\text{high}}$ , i.e.  $P_{\text{MCMC}}$  for  $\rho = \rho_3^{\text{IC}}$  and  $\rho_4^{\text{IC}}$  at  $T = T^{\text{IT}}$ . REFPROP uncertainty in  $P^{\text{high}}$  is  $\pm 1$  %.<sup>1,33</sup>

Pareto fronts, the Pareto optimal  $\lambda_{\text{CH}_3}$  value is either 15, 16, or 17, depending on the relative weight assigned to  $\rho_1^{\text{sat}}$  and  $P_v^{\text{sat}}$ . By contrast, since the  $\lambda_{\text{CH}_3} = 13, 14$ , and 18 Pareto fronts are completely inside the overall Pareto front, these  $\lambda_{\text{CH}_3}$  values are not optimal, regardless of the weighting.

Finally, and most importantly for our purposes, Figure 10 Panels b) and c) demonstrate the increase in MAPD% for  $\rho_1^{\text{sat}}$  and  $P_v^{\text{sat}}$  that accompanies more accurate prediction of  $P^{\text{high}}$ . For example, although  $\lambda_{\text{CH}_3} = 15, 16$ , and 17 are the best values based on VLE data, they over-predict  $P^{\text{high}}$  by around 10 %, 14 %, and 18 %, respectively. By contrast, while  $\lambda_{\text{CH}_3} = 13$  is the most accurate for  $P^{\text{high}}$ , the MAPD% for  $\rho_1^{\text{sat}}$  and  $P_v^{\text{sat}}$  are 4 and 40 times larger than the respective minimum MAPD%. These results support the fundamental claim of this work, namely, that the UA Mie  $\lambda$ -6 potential cannot adequately predict both VLE and high pressures for supercritical fluids and compressed liquids.

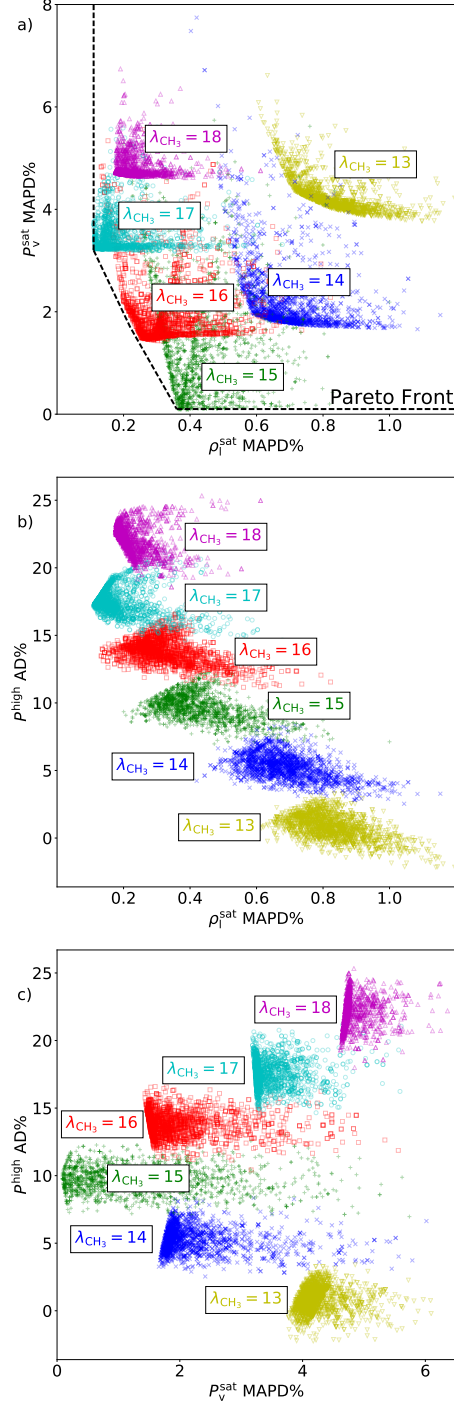


FIG. 10. Overall performance of  $\lambda_{CH_3} = 13$  to 18 for ethane. MCMC confirms that accurate prediction of VLE leads to large deviations in pressures for supercritical fluids and compressed liquids. Panel a) plots the mean absolute percent deviation (MAPD%) of  $\rho_{l,MCMC}^{sat}$  and  $P_{v,MCMC}^{sat}$ . Panels b) and c) plot the average deviation (AD%) in  $P^{high}$  with respect to MAPD% of  $\rho_{l,MCMC}^{sat}$  and  $P_{v,MCMC}^{sat}$ , respectively.

Figure 11 shows that UA Mie  $\lambda$ -6 potentials cannot predict both VLE and high pressure properties by comparing the Bayes factor for each value of  $\lambda_{\text{CH}_3}$  (normalized with respect to  $\lambda_{\text{CH}_3} = 14$ ) based solely on  $\rho_1^{\text{sat}}$  and  $P_v^{\text{sat}}$ . Bayes factors from 1 to 3.2, 3.2 to 10, 10 to 32, 32 to 100, and greater than 100 are typically classified as “not substantial”, “substantial”, “strong”, “very strong”, and “decisive” evidence, respectively.<sup>60</sup> With  $\frac{3.6}{0.02} = 180$ , there is “decisive” evidence against the use of  $\lambda_{\text{CH}_3} = 13$  for predicting  $\rho_1^{\text{sat}}$  and  $P_v^{\text{sat}}$ . As  $\lambda_{\text{CH}_3} = 13$  is the only value that predicts  $P^{\text{high}}$  within the REFPROP uncertainty, we conclude that no set of  $\epsilon_{\text{CH}_3}$ ,  $\sigma_{\text{CH}_3}$ , and  $\lambda_{\text{CH}_3}$  can predict *both* VLE and  $P^{\text{high}}$ .

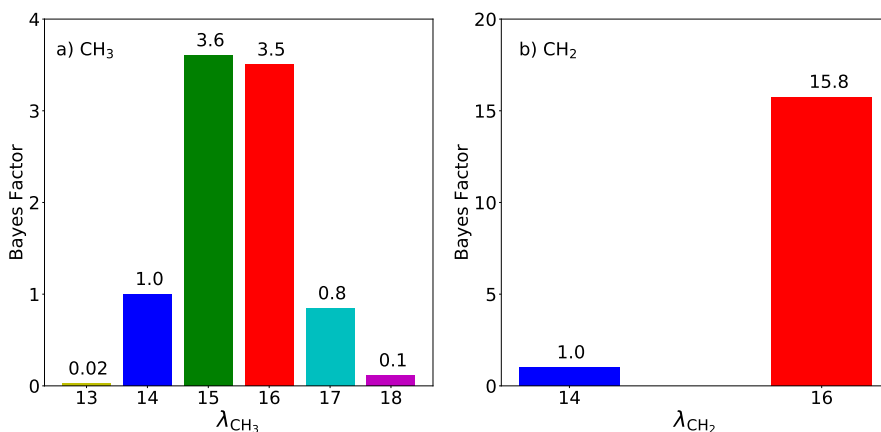


FIG. 11. Bayes Factor (evidence) for different values of  $\lambda_{\text{CH}_3}$  (Panel a) and  $\lambda_{\text{CH}_2}$  (Panel b). Evidence supports  $\lambda_{\text{CH}_3} = 15$  or  $16$  and  $\lambda_{\text{CH}_2} = 16$  over  $\lambda_{\text{CH}_2} = 14$ .  $\text{CH}_3$  values depend only on ethane while  $\text{CH}_2$  values are based on propane, *n*-butane, and *n*-octane. Note that all values are normalized with respect to  $\lambda = 14$ .

In addition, there is “very strong” evidence that the 18-6 potential is not justified by VLE data ( $\frac{3.6}{0.1} = 36$ ). The evidence in favor of the 15-6 or 16-6 potentials over the 14-6 and 17-6 potentials is not as definitive, although it is still considered “substantial” ( $\frac{3.6}{1.0}, \frac{3.6}{0.8}, \frac{3.5}{1.0}$ , and  $\frac{3.5}{0.8} > 3.5$ ). By contrast, the evidence for  $\lambda_{\text{CH}_3} = 15$  instead of  $\lambda_{\text{CH}_3} = 16$  is “not substantial” ( $\frac{3.6}{3.5} \approx 1.03$ ).

It is important to mention that these Bayes factors depend primarily on the VLE data and the  $s_{\text{D,SM}}^2$  model used to compute  $L(\theta|D)$ . We use a very conservative uncertainty



model for  $\rho_1^{\text{sat}}$  and  $P_v^{\text{sat}}$  (see Figure 6) so that our MCMC samples cover a large region of parameter space. This is done primarily to demonstrate that the UA Mie  $\lambda$ -6 is inadequate for predicting VLE and  $P^{\text{high}}$ . However, a less conservative uncertainty model would provide more convincing evidence regarding the optimal  $\lambda$  value based solely on VLE data.

Also, ITIC is limited to  $T^{\text{sat}} < 0.85T_c$ . Therefore, it is possible that the optimal value of  $\lambda_{\text{CH}_3}$  could be deduced (i.e. larger Bayes factors) if higher temperature VLE data were included (say from 260 to 290 K). Based on the observed bias in  $\rho_1^{\text{sat}}$  at higher temperatures (240 to 260 K) for  $\lambda_{\text{CH}_3} = 14$ , it appears that higher temperature VLE data would strengthen the counter evidence against the 14-6 potential. It is unclear whether higher temperature data would support the 15-6 or 16-6 potential, although the optimal  $\lambda_{\text{CH}_3}$  is likely a non-integer value between 15 and 16. Implementing MBAR with GCMC may be necessary to include VLE data from  $0.85 < T_r^{\text{sat}} < 0.95$ .

## B. Larger $n$ -alkanes

The conclusions regarding the UA Mie  $\lambda$ -6 potential for ethane are generally applicable to larger  $n$ -alkanes. Specifically, we observe that improved accuracy in predicting VLE requires a larger value of  $\lambda_{\text{CH}_2}$ . However, this improvement comes at the cost of significantly over-predicting  $P^{\text{high}}$ . Figure 12 presents the MCMC sampled  $\epsilon_{\text{CH}_2}$  and  $\sigma_{\text{CH}_2}$  parameter sets with Panels a) and b) corresponding to  $\lambda_{\text{CH}_2} = 16$  and  $\lambda_{\text{CH}_2} = 14$ , respectively. Note that these results were obtained using fixed values of  $\epsilon_{\text{CH}_3}$ ,  $\sigma_{\text{CH}_3}$ , and  $\lambda_{\text{CH}_3}$ , where  $\lambda_{\text{CH}_3} = \lambda_{\text{CH}_2}$ . The values of  $\epsilon_{\text{CH}_3}$  and  $\sigma_{\text{CH}_3}$  are the maximum likelihood parameter set from ethane for the corresponding  $\lambda_{\text{CH}_3}$  value.

Notice in Figure 12 that the MCMC sampled  $\epsilon_{\text{CH}_2}$  and  $\sigma_{\text{CH}_2}$  parameter sets, for a given value of  $\lambda_{\text{CH}_2}$ , overlap considerably for propane,  $n$ -butane, and  $n$ -octane. These joint-distributions provide statistical evidence in favor of the common assumption that  $\text{CH}_2$  parameters are transferable between different  $n$ -alkanes. To further demonstrate this point, Figure 12 includes the MCMC results when the posterior is based on the combined likelihoods from all three compounds, referred to as “MCMC transferable.”

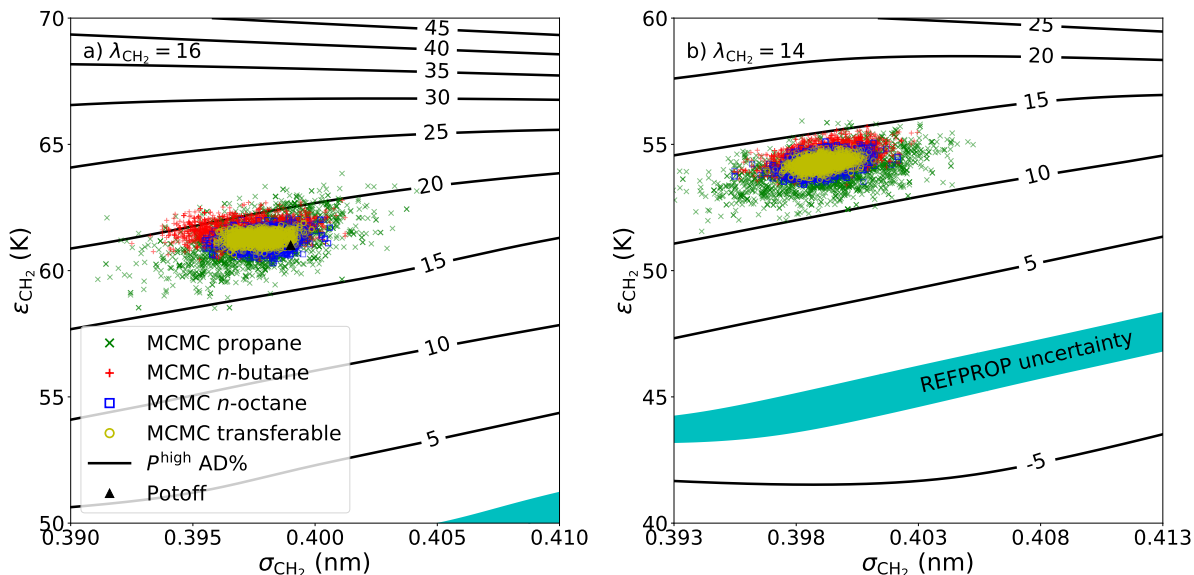


FIG. 12. High pressure performance of  $\lambda_{\text{CH}_2} = 16$  (Panel a) and 16 (Panel b) for propane, *n*-butane, and *n*-octane. MCMC sampled  $\epsilon_{\text{CH}_2}$  and  $\sigma_{\text{CH}_2}$  parameter sets result in large AD% for  $P^{\text{high}}$ . Contours are the AD% in  $P^{\text{high}}$  relative to the REFPROP values, where the “REFPROP uncertainty” region represents  $\pm 1\%$  deviation.<sup>1,34–36</sup> Panel a) includes the Potoff parameter set as a reference for  $\lambda_{\text{CH}_2} = 16$ .<sup>18</sup>

Panel a) shows that the Potoff  $\text{CH}_2$  parameter set is within the MCMC sample regions for  $\lambda_{\text{CH}_2} = 16$ . The same result was also observed for ethane (see Figure 7). This suggests that the Potoff  $\text{CH}_3$  and  $\text{CH}_2$  parameters are supported by the VLE data used in this study, even though the Potoff force field was parameterized using VLE data in a higher temperature range ( $0.6 < T_r^{\text{sat}} < 0.95$ ).

Also, note that the uncertainty in the parameters is largest for propane and smallest for *n*-octane. Therefore, the sensitivity of  $\rho_1^{\text{sat}}$  and  $P_v^{\text{sat}}$ , with respect to the  $\text{CH}_2$  parameters, increases with increasing number of  $\text{CH}_2$  interaction sites. Although this result is fairly intuitive, it is a valuable insight when selecting a training set of molecules for force field development. For example, notice that the MCMC transferable region is almost identical to that of *n*-octane, which shows that propane and *n*-butane data provide relatively little additional information that is not contained in the *n*-octane data.

Most importantly, for the purposes of this study, the contours in Figure 12 demonstrate that the MCMC sampled  $\epsilon_{\text{CH}_2}$  and  $\sigma_{\text{CH}_2}$  parameter sets have a strong positive bias (i.e. large AD%) in  $P^{\text{high}}$ . Specifically,  $\lambda_{\text{CH}_2} = 16$  and  $\lambda_{\text{CH}_2} = 14$  have AD% of approximately 16 % to 21 % and 10 % to 15 %, respectively, much greater than the REFPROP uncertainty of around 1 %. Furthermore, because the 0 % contour is roughly parallel to the MCMC region and found at much lower  $\epsilon_{\text{CH}_2}$  values, it is necessary to sacrifice considerable accuracy in  $\rho_1^{\text{sat}}$  and  $P_v^{\text{sat}}$  in order to accurately predict  $P^{\text{high}}$ . It is interesting that, for corresponding values of  $\lambda$ , the AD% for these larger  $n$ -alkanes is higher than that of ethane. This suggests that longer chain-lengths, with a UA Mie  $\lambda$ -6 force field, exacerbate the erroneous  $Z$  trend at high pressures.

Although the AD% in  $P^{\text{high}}$  is slightly lower for  $\lambda_{\text{CH}_2} = 14$  than for  $\lambda_{\text{CH}_2} = 16$ , the UA Mie 14-6 potential is significantly less reliable for VLE. Figure 11 demonstrates that there is “strong” evidence for  $\lambda_{\text{CH}_2} = 16$  over  $\lambda_{\text{CH}_2} = 14$ , based on VLE data. Note that the evidence in Figure 11 for the  $\lambda$  value of  $\text{CH}_2$  sites is stronger than that for the  $\text{CH}_3$  sites. This suggests that the ethane  $\rho_1^{\text{sat}}$  and  $P_v^{\text{sat}}$  results are less sensitive to  $\lambda$  than the larger  $n$ -alkanes and/or that the ethane VLE data contains less information than the combined data of propane,  $n$ -butane, and  $n$ -octane. In conclusion, these results suggest that neither UA Mie 16-6 or 14-6 force fields are capable of predicting VLE and  $P\rho T$  for supercritical fluids and compressed liquids of  $n$ -alkanes.

## VI. DISCUSSION

### A. Recommendations

Although the UA Mie  $\lambda$ -6 potential is not quantitatively reliable at high pressures, it may still be of use for FEOS parameterization when considering the insight gained in this study. For example, since the Potoff force field consistently over-predicts high pressures, a non-linear FEOS optimization could utilize the simulation results as an upper constraint for the FEOS pressure.<sup>3</sup> Furthermore, the primary purpose to include molecular simulation data for FEOS development is to increase the range of validity by ensuring

good behavior of the FEOS at high temperatures and pressures. While FEOS are based on empirical equations with 50 to 100 fitting parameters, even an inaccurate force field has a more sound theoretical basis. Therefore, the UA Mie  $\lambda$ -6 simulation output for a given property should not demonstrate non-physical oscillations, inflection points, derivative sign-changes, etc., which can plague a poorly-fit FEOS.

Essentially, whether or not a FEOS should be developed using a hybrid data set consisting of UA Mie  $\lambda$ -6 simulation results depends on the quality and quantity of available experimental data. If the data cover a wide range of state points and properties, it is possible that the UA Mie  $\lambda$ -6 potential may still be useful, despite the systematic deviations at high pressures. By contrast, if the experimental data are limited such that the FEOS depends almost entirely on the molecular simulation results, the UA Mie  $\lambda$ -6 force field will lead to large deviations at high pressures. Therefore, in this scenario, we advise against the use of UA Mie  $\lambda$ -6 force fields when developing a FEOS for normal and branched alkanes. For this purpose, we recommend further investigation of alternative potentials with a softer repulsive barrier and a more sound theoretical basis, e.g. Buckingham exponential-6, modified-Morse,<sup>28–30</sup> or an extended Lennard-Jones.<sup>43,61,62</sup>

## B. Limitations

There are some caveats to the primary conclusion from this study that UA Mie  $\lambda$ -6 force fields parameterized with VLE data should not be used to develop fundamental equations of state for normal and branched alkanes. The main limitation is that the poor extrapolation at high pressures is based solely on the trend of  $Z$  with respect to inverse temperature. By contrast, the simulation values that are typically included in hybrid data sets used to generate FEOS are derivatives of the departure (or residual) Helmholtz free energy with respect to inverse temperature and/or density:<sup>7–11</sup>

$$A_{xy}^{\text{dep}} R_g T \equiv (1/T)^x \rho^y \frac{\partial^{x+y} A^{\text{dep}}}{\partial (1/T)^x \partial \rho^y} \quad (25)$$

where  $x$  and  $y$  are integer values and the derivative is of order  $x + y$ . There are advantages of using  $A_{xy}^{\text{dep}}$  for developing FEOS, as this approach eliminates redundant information

found in traditional macroscopic properties.<sup>2,4-7</sup> For example, the following expressions demonstrate the interdependency of the properties we computed, namely,  $Z$  and  $U^{\text{dep}}$  with their derivatives along isochores and isotherms:<sup>6</sup>

$$Z = 1 + A_{01}^{\text{dep}} \quad (26)$$

$$\frac{1}{T} \left( \frac{-\partial Z}{\partial(1/T)} \right)_{\rho} = 1 + A_{01}^{\text{dep}} - A_{11}^{\text{dep}} \quad (27)$$

$$\frac{U^{\text{dep}}}{R_g T} = A_{10}^{\text{dep}} \quad (28)$$

$$\frac{1}{R_g} \left( \frac{\partial U^{\text{dep}}}{\partial T} \right)_{\rho} = -A_{20}^{\text{dep}} \quad (29)$$

$$\rho \left( \frac{\partial Z}{\partial \rho} \right)_T = 1 + 2A_{01}^{\text{dep}} + A_{02}^{\text{dep}} \quad (30)$$

However, at least two reasons exist as for why the conclusions of this study are not based on  $A_{xy}^{\text{dep}}$ . First, with the exception of *ms2*,<sup>63</sup> we are not aware of any open-source simulation package that readily provides  $A_{xy}^{\text{dep}}$ . As *ms2* is currently limited to small rigid molecules it is not amenable to the systems of interest. In addition, macroscopic properties, such as  $Z$  and  $U^{\text{dep}}$  (with their respective derivatives), are more readily understood and visualized than  $A_{xy}^{\text{dep}}$ . Also, it is easier to quantify their impact on process design than derivatives in the residual Helmholtz free energy. For example, as demonstrated in Reference 8, an inaccurate prediction of some  $A_{xy}^{\text{dep}}$  does not necessarily result in poor prediction of  $P\rho T$  behavior or heat capacities.

Although we do not perform a detailed investigation of  $A_{xy}^{\text{dep}}$ , we have indirectly investigated each of the  $A_{xy}^{\text{dep}}$  terms in Equations 26-30. For example, Sections III and V present  $Z$  and, by inspection, the slope of  $Z$  with respect to  $1/T$  at constant  $\rho$ . Since these properties are equivalent to Equations 26 and 27, respectively, Sections III and V indirectly focus on two of the Helmholtz derivatives, namely,  $A_{01}^{\text{dep}}$  and  $A_{11}^{\text{dep}}$ . Section SI.V of Supporting Information also demonstrates some deviations in  $U^{\text{dep}}$ , the slope of  $U^{\text{dep}}$  with respect to  $T$  at constant  $\rho$ , and the slope of  $Z$  with respect to  $\rho$  at constant  $T$ , which are equivalent to Equations 28-30. Unfortunately, although these additional properties provide insight regarding  $A_{10}^{\text{dep}}$ ,  $A_{20}^{\text{dep}}$ ,  $A_{01}^{\text{dep}}$ , and  $A_{02}^{\text{dep}}$ , the results are less conclusive due to the relatively

large uncertainties in the REFPROP values, ca. 5 % and 10 % for  $U^{\text{dep}}$  and  $\left(\frac{\partial U^{\text{dep}}}{R_g \partial T}\right)_\rho$ , respectively. Furthermore, the relationship between Equations 28-30 and the repulsive barrier,  $\lambda$ , is not obvious from these results. Future work should investigate more thoroughly the adequacy of UA Mie  $\lambda$ -6 (or other) force fields to predict  $U^{\text{dep}}$  and isochoric/isobaric heat capacities at high temperatures and pressures.

Another potential limitation is that we utilize a single layer Bayes model as opposed to a hierarchical model, where the posterior is proportional to multiple priors that depend on the parameters from different levels of the hierarchy (for a more detailed discussion see References 31 and 50). Wu et al. demonstrated the need for hierarchical models when the data set,  $D$ , contains discrepancies, i.e. internal inconsistencies. However, since we use a conservative estimate for the surrogate model uncertainty, i.e.  $u_{\text{SM}} \gg u_D$ , any discrepancies in the VLE data should not affect the parameter uncertainties. A hierarchical approach is also useful when accounting for model inadequacies, i.e. when the force field is not capable of representing multiple data types. A hierarchical method should thus be favored if determining the parameter uncertainty when simultaneously considering  $\rho_1^{\text{sat}}$ ,  $P_v^{\text{sat}}$  and  $P^{\text{high}}$ . Furthermore, a hierarchical model should be used if the parameters are not transferable between molecules, e.g. the Potoff CH and C parameters for “short” and “long” branched alkanes. However, such a hierarchical approach is unnecessary for our purposes, since the transferable UA Mie  $\lambda$ -6 force field for  $n$ -alkanes is capable of reproducing  $\rho_1^{\text{sat}}$  and  $P_v^{\text{sat}}$ , which are the only properties included in  $D$ .

## VII. CONCLUSIONS

Recently, molecular simulation results at extreme temperatures and pressures have supplemented experimental data when developing fundamental equations of state for compounds with limited experimental data. For this hybrid data set approach to work, it is imperative that the force field be reliable and transferable over different  $P\rho T$  conditions. Unfortunately, literature united-atom force fields that are highly accurate for estimating VLE properties of normal and branched alkanes have systematic deviations in  $Z$  at non-VLE conditions. Bayesian inference suggests that the UA Mie  $\lambda$ -6 model type

is not adequate for simultaneously predicting  $\rho_l^{\text{sat}}$ ,  $P_v^{\text{sat}}$ , and  $P^{\text{high}}$ . In the case of ethane, evidence from VLE data supports  $\lambda = 15$  or 16, while  $Z$  at high pressures requires  $\lambda = 13$ . A similar trend is observed for larger  $n$ -alkanes. Specifically, evidence from VLE data supports  $\lambda = 16$ , while we observe only slight improvement in  $Z$  at high pressures for  $\lambda = 14$ . Therefore, while considerable improvement in VLE is observed for the Mie  $\lambda$ -6 potential over the traditional Lennard-Jones 12-6, the use of  $\lambda > 12$  does not appear to have physical/theoretical justification but, rather, is simply an empirical remedy that performs well for VLE. For these reasons, we recommend that alternative models be considered for developing FEOS of normal and branched alkanes, such as force fields that use anisotropic-united-atom, all-atom, and/or alternative non-bonded potentials.

## ACKNOWLEDGMENTS

We are appreciative for the assistance provided by Eric W. Lemmon regarding the reliability and uncertainties of the REFPROP correlations at high pressures. We would also like to acknowledge the Bayesian expertise provided by Joshua H. Fass of the Chodera lab at the Memorial Sloan Kettering Cancer Center. We are grateful for the internal review provided by Ian H. Bell and Daniel W. Siderius from the National Institute of Standards and Technology (NIST).

This research was performed while Richard A. Messerly held a National Research Council (NRC) Postdoctoral Research Associateship at NIST. Michael R. Shirts acknowledges support from National Science Foundation (NSF) grant CHE-1738975.

## REFERENCES

- <sup>1</sup>E. W. Lemmon, M. L. Huber, and M. O. McLinden. NIST Standard Reference Database 23: Reference Fluid Thermodynamic and Transport Properties-REFPROP, Version 9.1, National Institute of Standards and Technology, 2013.
- <sup>2</sup>Monika Thol, Gábor Rutkai, Andreas Köster, Rolf Lustig, Roland Span, and Jadran

- Vrabec. Equation of state for the Lennard-Jones fluid. *Journal of Physical and Chemical Reference Data*, 45(2):023101, 2016.
- <sup>3</sup>Monika Thol, Gábor Rutkai, Roland Span, Jadran Vrabec, and Rolf Lustig. Equation of state for the Lennard-Jones truncated and shifted model fluid. *International Journal of Thermophysics*, 36(1):25–43, 2015.
- <sup>4</sup>Gábor Rutkai, Monika Thol, Roland Span, and Jadran Vrabec. How well does the Lennard-Jones potential represent the thermodynamic properties of noble gases? *Molecular Physics*, 115(9-12):1104–1121, 2017.
- <sup>5</sup>Rolf Lustig, Gábor Rutkai, and Jadran Vrabec. Thermodynamic correlation of molecular simulation data. *Molecular Physics*, 113(9-10):910–931, 2015.
- <sup>6</sup>Gábor Rutkai and Jadran Vrabec. Empirical fundamental equation of state for phosgene based on molecular simulation data. *Journal of Chemical & Engineering Data*, 60(10):2895–2905, 2015.
- <sup>7</sup>G. Rutkai, M. Thol, R. Lustig, R. Span, and J. Vrabec. Communication: Fundamental equation of state correlation with hybrid data sets. *The Journal of Chemical Physics*, 139(4):041102, 2013.
- <sup>8</sup>M. Thol, F.H. Dubberke, G. Rutkai, T. Windmann, A. Köster, R. Span, and J. Vrabec. Fundamental equation of state correlation for hexamethyldisiloxane based on experimental and molecular simulation data. *Fluid Phase Equilibria*, 418:133 – 151, 2016. Special Issue covering the Nineteenth Symposium on Thermophysical Properties.
- <sup>9</sup>Monika Thol, Gábor Rutkai, Andreas Köster, Frithjof H. Dubberke, Thorsten Windmann, Roland Span, and Jadran Vrabec. Thermodynamic properties of octamethylcyclotetrasiloxane. *Journal of Chemical & Engineering Data*, 61(7):2580–2595, 2016.
- <sup>10</sup>Monika Thol, Gábor Rutkai, Andreas Köster, Svetlana Miroshnichenko, Wolfgang Wagner, Jadran Vrabec, and Roland Span. Equation of state for 1,2-dichloroethane based on a hybrid data set. *Molecular Physics*, 115(9-12):1166–1185, 2017.
- <sup>11</sup>Monika Thol, Gábor Rutkai, Andreas Köster, Mirco Kortmann, Roland Span, and Jadran Vrabec. Fundamental equation of state for ethylene oxide based on a hybrid dataset. *Chemical Engineering Science*, 121:87 – 99, 2015. 2013 Danckwerts Special Issue on Molecular Modelling in Chemical Engineering.



- <sup>12</sup>M. G. Martin and J. I. Siepmann. Transferable potentials for phase equilibria. 1. United-atom description of n-alkanes. *The Journal of Physical Chemistry B*, 102(14):2569–2577, 1998.
- <sup>13</sup>Marcus G. Martin and J. Ilja Siepmann. Novel configurational-bias monte carlo method for branched molecules. Transferable Potentials for Phase Equilibria. 2. United-Atom Description of Branched Alkanes. *The Journal of Physical Chemistry B*, 103(21):4508–4517, 1999.
- <sup>14</sup>Mansi S. Shah, J. Ilja Siepmann, and Michael Tsapatsis. Transferable potentials for phase equilibria. Improved united-atom description of ethane and ethylene. *AIChE Journal*, 63(11):5098–5110, 2017.
- <sup>15</sup>J. R. Errington and A. Z. Panagiotopoulos. A new intermolecular potential model for the n-alkane homologous series. *The Journal of Physical Chemistry B*, 103(30):6314–6322, 1999.
- <sup>16</sup>Philippe Ungerer, Christele Beauvais, Jerome Delhommelle, Anne Boutin, Bernard Rousseau, and Alain H. Fuchs. Optimization of the anisotropic united atoms intermolecular potential for n-alkanes. *The Journal of Chemical Physics*, 112(12):5499–5510, 2000.
- <sup>17</sup>Emeric Bourasseau, Philippe Ungerer, Anne Boutin, and Alain H. Fuchs. Monte carlo simulation of branched alkanes and long chain n-alkanes with anisotropic united atoms intermolecular potential. *Molecular Simulation*, 28(4):317–336, 2002.
- <sup>18</sup>J. J. Potoff and D. A. Bernard-Brunel. Mie potentials for phase equilibria calculations: Applications to alkanes and perfluoroalkanes. *The Journal of Physical Chemistry B*, 113(44):14725–14731, 2009.
- <sup>19</sup>Jason R. Mick, Mohammad Soroush Barhaghi, Brock Jackman, Loren Schwiebert, and Jeffrey J. Potoff. Optimized mie potentials for phase equilibria: Application to branched alkanes. *Journal of Chemical & Engineering Data*, 62(6):1806–1818, 2017.
- <sup>20</sup>Andrea Hemmen and Joachim Gross. Transferable anisotropic united-atom force field based on the Mie potential for phase equilibrium calculations: n-alkanes and n-olefins. *The Journal of Physical Chemistry B*, 119(35):11695–11707, 2015.
- <sup>21</sup>Dominik Weidler and Joachim Gross. Transferable anisotropic united-atom force field

- based on the mie potential for phase equilibria: Aldehydes, ketones, and small cyclic alkanes. *Industrial & Engineering Chemistry Research*, 55(46):12123–12132, 2016.
- <sup>22</sup>Carmelo Herdes, Tim S. Totton, and Erich A. Müller. Coarse grained force field for the molecular simulation of natural gases and condensates. *Fluid Phase Equilibria*, 406:91 – 100, 2015.
- <sup>23</sup>K. Stöbener, P. Klein, M. Horsch, K. Kufer, and H. Hasse. Parametrization of two-center Lennard-Jones plus point-quadrupole force field models by multicriteria optimization. *Fluid Phase Equilibria*, 411:33 – 42, 2016.
- <sup>24</sup>Richard A. Messerly, Thomas A. Knotts IV, and W. Vincent Wilding. Uncertainty quantification and propagation of errors of the Lennard-Jones 12-6 parameters for n-alkanes. *The Journal of Chemical Physics*, 146(19):194110, 2017.
- <sup>25</sup>M. P. Allen and D. J. Tildesley. *Computer Simulation of Liquids*. Clarendon Press ; Oxford University Press, Oxford England New York, 1987.
- <sup>26</sup>Peter A. Gordon. Development of intermolecular potentials for predicting transport properties of hydrocarbons. *The Journal of Chemical Physics*, 125(1):014504, 2006.
- <sup>27</sup>Guillaume Galliéro, Christian Boned, Antoine Baylaucq, and François Montel. Molecular dynamics comparative study of Lennard-Jones  $\alpha$ -6 and exponential  $\alpha$ -6 potentials: Application to real simple fluids (viscosity and pressure). *Phys. Rev. E*, 73:061201, 2006.
- <sup>28</sup>Richard L. Rowley and Tapani Pakkanen. Determination of a methane intermolecular potential model for use in molecular simulations from ab initio calculations. *The Journal of Chemical Physics*, 110(7):3368–3377, 1999.
- <sup>29</sup>Richard L. Rowley, Yan Yang, and Tapani A. Pakkanen. Determination of an ethane intermolecular potential model for use in molecular simulations from ab initio calculations. *The Journal of Chemical Physics*, 114(14):6058–6067, 2001.
- <sup>30</sup>Joseph M. Hayes, James C. Greer, and David A. Morton-Blake. A force-field description of short-range repulsions for high density alkane molecular dynamics simulations. *Journal of Computational Chemistry*, 25(16):1953–1966, 2004.
- <sup>31</sup>Lina Kulakova, Georgios Arampatzis, Panagiotis Angelikopoulos, Panagiotis Hadjidakas, Costas Papadimitriou, and Petros Koumoutsakos. Data driven inference for the repulsive exponent of the Lennard-Jones potential in molecular dynamics simula-

- tions. *Scientific Reports*, 7(1):16576, 2017.
- <sup>32</sup>Jason R. Mick, Mohammad Soroush Barhaghi, Brock Jackman, Kamel Rushaidat, Loren Schwiebert, and Jeffrey J. Potoff. Optimized Mie potentials for phase equilibria: Application to noble gases and their mixtures with n-alkanes. *The Journal of Chemical Physics*, 143(11):114504, 2015.
- <sup>33</sup>D. Bücker and W. Wagner. A reference equation of state for the thermodynamic properties of ethane for temperatures from the melting line to 675 K and pressures up to 900 MPa. *Journal of Physical and Chemical Reference Data*, 35(1):205–266, 2006.
- <sup>34</sup>Eric W. Lemmon, Mark O. McLinden, and Wolfgang Wagner. Thermodynamic properties of propane. iii. a reference equation of state for temperatures from the melting line to 650 K and pressures up to 1000 MPa. *Journal of Chemical & Engineering Data*, 54(12):3141–3180, 2009.
- <sup>35</sup>D. Bücker and W. Wagner. Reference equations of state for the thermodynamic properties of fluid phase n-butane and isobutane. *Journal of Physical and Chemical Reference Data*, 35(2):929–1019, 2006.
- <sup>36</sup>R. Beckmueller, M. Thol, and R. Span. Fundamental equation of state for n-octane. *International Journal of Thermophysics*, Pending publication, 2018.
- <sup>37</sup>Eric W. Lemmon and Roland Span. Short fundamental equations of state for 20 industrial fluids. *Journal of Chemical & Engineering Data*, 51(3):785–850, 2006.
- <sup>38</sup>T.M. Blackham, A.K. Lemmon, and E.W. Lemmon. Fundamental equation of state for isooctane. *International Journal of Thermophysics*, Pending publication, 2018.
- <sup>39</sup>M.J. Abraham, D. van der Spoel, E. Lindahl, B.Hess, and the GROMACS development team. *GROMACS User Manual version 2018*, [www.gromacs.org](http://www.gromacs.org) (2018), 2018.
- <sup>40</sup>William G. Hoover. Canonical dynamics: Equilibrium phase-space distributions. *Physical Review A*, 31:1695–1697, 1985.
- <sup>41</sup>Berk Hess, Henk Bekker, Herman J. C. Berendsen, and Johannes G. E. M. Fraaije. LINCS: A linear constraint solver for molecular simulations. *Journal of Computational Chemistry*, 18(12):1463–1472, 1998.
- <sup>42</sup>Berk Hess. P-LINCS: A parallel linear constraint solver for molecular simulation. *Journal of Chemical Theory and Computation*, 4(1):116–122, 2008.

- <sup>43</sup>Seyed Mostafa Razavi. Optimization of a transferable shifted force field for interfaces and inhomogeneous fluids using thermodynamic integration. Master's thesis, The University of Akron, 2016.
- <sup>44</sup>Richard A. Messerly, S. Mostafa Razavi, and Michael R. Shirts. Configuration-sampling-based surrogate models for rapid parameterization of non-bonded interactions. *Journal of Chemical Theory and Computation*, 14(6):3144–3162, 2018.
- <sup>45</sup>S. Mostafa Razavi, Richard A. Messerly, and J. Richard Elliott. Coexistence calculation using the isothermal-isochoric integration method. Pending publication., 2018.
- <sup>46</sup>Carlos Nieto-Draghi, Anthony Bocahut, Benoît Creton, Pascal Have, Aziz Ghoufi, Aurélie Wender, , Anne Boutin, Bernard Rousseau, and Laurent Normand. Optimisation of the dynamical behaviour of the anisotropic united atom model of branched alkanes: application to the molecular simulation of fuel gasoline. *Molecular Simulation*, 34(2):211–230, 2008.
- <sup>47</sup>F. Rizzi, H. N. Najm, B. J. Debusschere, K. Sargsyan, M. Salloum, H. Adalsteinsson, and O. M. Knio. Uncertainty quantification in MD simulations. Part II: Bayesian inference of force-field parameters. *Multiscale Modeling & Simulation*, 10(4):1460–1492, 2012.
- <sup>48</sup>Panagiotis Angelikopoulos, Costas Papadimitriou, and Petros Koumoutsakos. Bayesian uncertainty quantification and propagation in molecular dynamics simulations: A high performance computing framework. *The Journal of Chemical Physics*, 137(14):144103, 2012.
- <sup>49</sup>Fabien Cailliez and Pascal Pernot. Statistical approaches to forcefield calibration and prediction uncertainty in molecular simulation. *The Journal of Chemical Physics*, 134(5):054124, 2011.
- <sup>50</sup>S. Wu, P. Angelikopoulos, C. Papadimitriou, R. Moser, and P. Koumoutsakos. A hierarchical bayesian framework for force field selection in molecular dynamics simulations. *Philosophical Transactions of the Royal Society of London A: Mathematical, Physical and Engineering Sciences*, 374(2060), 2016.
- <sup>51</sup>Michael R. Shirts and John D. Chodera. Statistically optimal analysis of samples from multiple equilibrium states. *The Journal of Chemical Physics*, 129:124105, 2008.
- <sup>52</sup>A. Vetere. The Riedel equation. *Industrial & Engineering Chemistry Research*, 30(11):2487–

2492, 1991.

- <sup>53</sup>M. Funke, R. Kleinrahm, and W. Wagner. Measurement and correlation of the ( $P$ ,  $\rho$ ,  $T$ ) relation of ethane II. Saturated-liquid and saturated-vapour densities and vapour pressures along the entire coexistence curve. *The Journal of Chemical Thermodynamics*, 34(12):2017 – 2039, 2002.
- <sup>54</sup>Levi N. Naden and Michael R Shirts. Rapid computation of thermodynamic properties over multidimensional nonbonded parameter spaces using adaptive multistate reweighting. *Journal of Chemical Theory and Computation*, 12(4):1806–1823, 2016.
- <sup>55</sup>Paul N. Patrone, Andrew Dienstfrey, Andrea R. Browning, Samuel Tucker, and Stephen Christensen. Uncertainty quantification in molecular dynamics studies of the glass transition temperature. *Polymer*, 87:246 – 259, 2016.
- <sup>56</sup>Michael Schappals, Andreas Mecklenfeld, Leif Kröger, Vitalie Botan, Andreas Köster, Simon Stephan, Edder J. García, Gábor Rutkai, Gabriele Raabe, Peter Klein, Kai Leonhard, Colin W. Glass, Johannes Lenhard, Jadran Vrabec, and Hans Hasse. Round robin study: Molecular simulation of thermodynamic properties from models with internal degrees of freedom. *Journal of Chemical Theory and Computation*, 13(9):4270–4280, 2017.
- <sup>57</sup>Michael Frenkel, Robert D. Chirico, Vladimir Diky, Xinjian Yan, Qian Dong, and Chris Muzny. Thermodata engine (TDE): software implementation of the dynamic data evaluation concept. *Journal of Chemical Information and Modeling*, 45(4):816–838, 2005.
- <sup>58</sup>K. Stöbener, P. Klein, S. Reiser, M. Horsch, K.-H. Kufer, and H. Hasse. Multicriteria optimization of molecular force fields by Pareto approach. *Fluid Phase Equilibria*, 373:100 – 108, 2014.
- <sup>59</sup>Stephan Werth, Katrin Stöbener, Peter Klein, Karl-Heinz Kufer, Martin Horsch, and Hans Hasse. Molecular modelling and simulation of the surface tension of real quadrupolar fluids. *Chemical Engineering Science*, 121:110 – 117, 2015. 2013 Danckwerts Special Issue on Molecular Modelling in Chemical Engineering.
- <sup>60</sup>Harold Jeffreys. *The Theory of Probability. Third edition*. Clarendon Press: Oxford, 2004.
- <sup>61</sup>Photos G. Hajigeorgiou. The extended Lennard-Jones potential energy function: A simpler model for direct-potential-fit analysis. *Journal of Molecular Spectroscopy*, 330:4 – 13, 2016. Potentiology and Spectroscopy in Honor of Robert Le Roy.

- <sup>62</sup>Ferenc Kalos and Arthur E. Grosser. Intermolecular potentials from differential cross sections: Ar + Ar. *Canadian Journal of Chemistry*, 50(6):892–896, 1972.
- <sup>63</sup>Gábor Rutkai, Andreas Köster, Gabriela Guevara-Carrion, Tatjana Janzen, Michael Schappals, Colin W. Glass, Martin Bernreuther, Amer Wafai, Simon Stephan, Maximilian Kohns, Steffen Reiser, Stephan Deublein, Martin Horsch, Hans Hasse, and Jadran Vrabec. ms2: A molecular simulation tool for thermodynamic properties, release 3.0. *Computer Physics Communications*, 221:343 – 351, 2017.